



RESEARCH ARTICLE OPEN ACCESS

A Dynamic Implicit 3D Material Point-To-Rigid Body Contact Approach for Large Deformation Analysis

Robert E. Bird¹  | Giuliano Pretti¹  | William M. Coombs¹ | Charles E. Augarde¹ | Yaseen U. Sharif² | Michael J. Brown² | Gareth Carter^{3,4} | Catriona Macdonald⁴ | Kirstin Johnson⁴

¹Department of Engineering, Durham University, Durham, UK | ²School of Science and Engineering, University of Dundee, Dundee, UK | ³Arup, Edinburgh, UK | ⁴British Geological Survey, Currie, Edinburgh, UK

Correspondence: William M. Coombs (w.m.coombs@durham.ac.uk)

Received: 20 March 2025 | **Revised:** 31 March 2025 | **Accepted:** 24 June 2025

Funding: This work was supported by the Engineering and Physical Sciences Research Council (Grant Nos. EP/W000970/1, EP/W000954/1, and EP/W000997/1). The second author is also supported by funding from the Faculty of Science, Durham University.

Keywords: contact mechanics | implicit dynamics | large deformation mechanics | material point method | soil-structure interaction

ABSTRACT

Accurate and robust modeling of large deformation three-dimensional contact interaction is an important area of engineering, but it is also challenging from a computational mechanics perspective. This is particularly the case when there is significant interpenetration and evolution of the contact surfaces, such as the case of a relatively rigid body interacting with a highly deformable body. This paper provides a new three-dimensional large deformation contact approach where the Material Point Method (MPM) is used to represent the deformable material. A new contact detection approach is introduced that checks the interaction of the vertices of the domains associated with each material point with the discretized rigid body. This provides a general and consistent approach without requiring the reconstruction of an additional boundary representation of the deformable body. A new energy-consistent material point domain updating approach is also introduced that maintains stable simulations under large deformations. The dynamic governing equations allow the trajectory of the rigid body to evolve based on the interaction with the deformable body, and the governing equations are solved within an efficient implicit framework. The performance of the new contact approach is demonstrated on a number of benchmark problems with analytical solutions. The method is also applied to the specific case of soil-structure interaction, using geotechnical centrifuge experimental data that confirms the veracity of the proposed approach.

1 | Introduction

Modeling the interaction between deformable bodies under large deformations requires robust contact algorithms that are able to track and handle the evolving contact surfaces while enforcing the required contact constraints. In many areas of engineering, one of the bodies can be very stiff compared to the other, which permits a rigid body assumption for the stiffer material. One such

application area is soil-structure interaction, which is a key area of geotechnical engineering, particularly in offshore geotechnics, where almost all interactions with the seabed involve large deformation processes. This paper focuses on such problems and, building on the work of Bird et al. [1], adopts the Material Point Method (MPM [2]), as the numerical method to represent soil behavior due to the MPM's established track record of modeling large deformation geotechnical problems (see Solowski et al.

This is an open access article under the terms of the [Creative Commons Attribution](https://creativecommons.org/licenses/by/4.0/) License, which permits use, distribution and reproduction in any medium, provided the original work is properly cited.

© 2025 The Author(s). *International Journal for Numerical Methods in Engineering* published by John Wiley & Sons Ltd.

[3] and de Vaucorbeil et al. [4] for review articles). The implicit dynamic MPM formulation used in this paper is outlined in Section 2.

There are numerous choices in terms of how to enforce contact between the soil and the structure. The original MPM includes a form of no-slip contact in that multiple bodies interact on a shared background grid, where the governing equations are assembled and solved. However, most of these methods struggle to rigorously enforce contact as they lack an explicit definition of the contact surface between the bodies [5, 6]. The focus in this paper is on soil-structure interaction where the stiffness of the structure is sufficiently large, relative to the deformable soil body, that it can be assumed to be rigid. This allows the contact surface to be based on the geometry of the rigid body [1]. Therefore, this introduction outlines specific MPM contributions that focus on soil-structure interaction with a clearly defined contact boundary rather than attempt to provide a comprehensive review of all MPM-based contact formulations (see Bird et al. [1] for a more detailed overview). Within this context, Nakamura et al. [7] used the boundary discretization of an infinitely rigid body to define the contact surface, while Lei et al. [8] employed a finite element discretization that allowed the structure to deform whilst providing an explicit representation of the contact surface. It is worth noting that in some cases it is possible to maintain a rigid body conforming background mesh, which allows the contact constraints to be imposed directly on the background grid (see, e.g., Martinelli and Vahid [9]). However, in all but the simplest of cases this necessitates the use of unstructured background grids, usually simplex elements, which causes other issues such as cell crossing instabilities as MPM formulations adopting C_1 continuous basis functions (such as generalized interpolation [10] and B-spline [11] basis functions) are only available for structured grids. This paper extends the two-dimensional quasi-static contact approach of Bird et al. [1] to three-dimensional dynamic analysis, including coupled soil reaction dependent rigid body motion. The deformable body is represented by Generalized Interpolation Material Points (GIMPs) to mitigate cell crossing instabilities. Numerical methods for enforcing contact constraints can be broadly grouped into penalty, augmented Lagrangian, and Lagrange multiplier methods [12]. Again following Bird et al. [1], here the geometrically non-linear contact constraints are enforced via a penalty approach, and the dynamic coupled soil deformation-rigid body motion equations are resolved using an implicit monolithic solver. The contact detection and enforcement algorithm is based on the interaction between the rigid body and the generalized interpolation domain associated with each material point. This means that the contact penalty forces are consistent with the internal forces generated based on the stress state of material points and that no additional material point-based boundary representation is required. Details of the approach are covered in Sections 3, 4, and 5, which provide a description of the rigid body, details of the contact formulation, and information on specific aspects of the numerical implementation, respectively.

The key contribution of this paper is a new three-dimensional MPM-based soil-structure interaction approach for dynamic problems that allows for the motion of the structure to evolve based on the response of the deformable body. This is important for several areas of offshore geotechnical engineering where

the motion of the rigid body is only partially prescribed. Solving the coupled equations implicitly permits the use of large time steps compared to most of the MPM literature that focuses on explicit solution methods. Enforcing the contact constraints based on the domains associated with each material point provides a robust, general, and consistent soil-structure interaction approach. The advantages of the proposed formulation are demonstrated by a number of benchmark and exemplar test cases.

2 | Material Point Method

To avoid mesh distortion issues seen in other mesh-based methods, the MPM requires two spatial discretizations: Material points representing the physical body and a background grid to solve the governing equations. A typical time step in the MPM can be broken down as shown in Figure 1:

- a. *Initial position*: At the start of an analysis the physical body being analyzed (shown by the light grey shaded region with a boundary defined by the black line) is discretized as a collection of material points (shown by the dark grey shaded circles) with associated volume, mass and constitutive parameters (e.g., Young's modulus). The body lies within a background grid of sufficient size to cover the full extent of the material points.
- b. *Point-to-grid mapping*: Information held at material points, such as mass, stiffness, and forces associated with gravitational loads, any tractions applied to material points, and the stress in the material, is mapped to the nodes of the background grid.
- c. *Governing equation assembly*: The governing equations describing the physical problem being analyzed are assembled at the degrees of freedom of the background grid. This leads to a finite element-like system of equations, which will change size depending on the interaction between the material points and the grid, as only some nodes will be *active* in the analysis (those with contributions from material points, as shown by the white shaded circles).
- d. *Grid solution*: The governing equations, combined with any boundary conditions imposed directly on the grid or from immersed constraints, are solved at the *active* degrees of freedom to determine the primary unknowns of the system of equations (for static and dynamic stress analysis this would usually be displacements and accelerations, respectively). How the equations are solved defines different MPMs and depends on the nature of the equations and the adopted time stepping algorithm.
- e. *Grid-to-point mapping*: The solution is mapped from the grid to the material points, such as displacement, velocity, stress, deformation, volume, etc.
- f. *Point/grid update*: The positions of the material points are updated, and the background grid is reset or replaced.

These steps describe a general material point time step for quasi-static or dynamic stress analysis problems. Details of the calculation steps will change depending on the solution

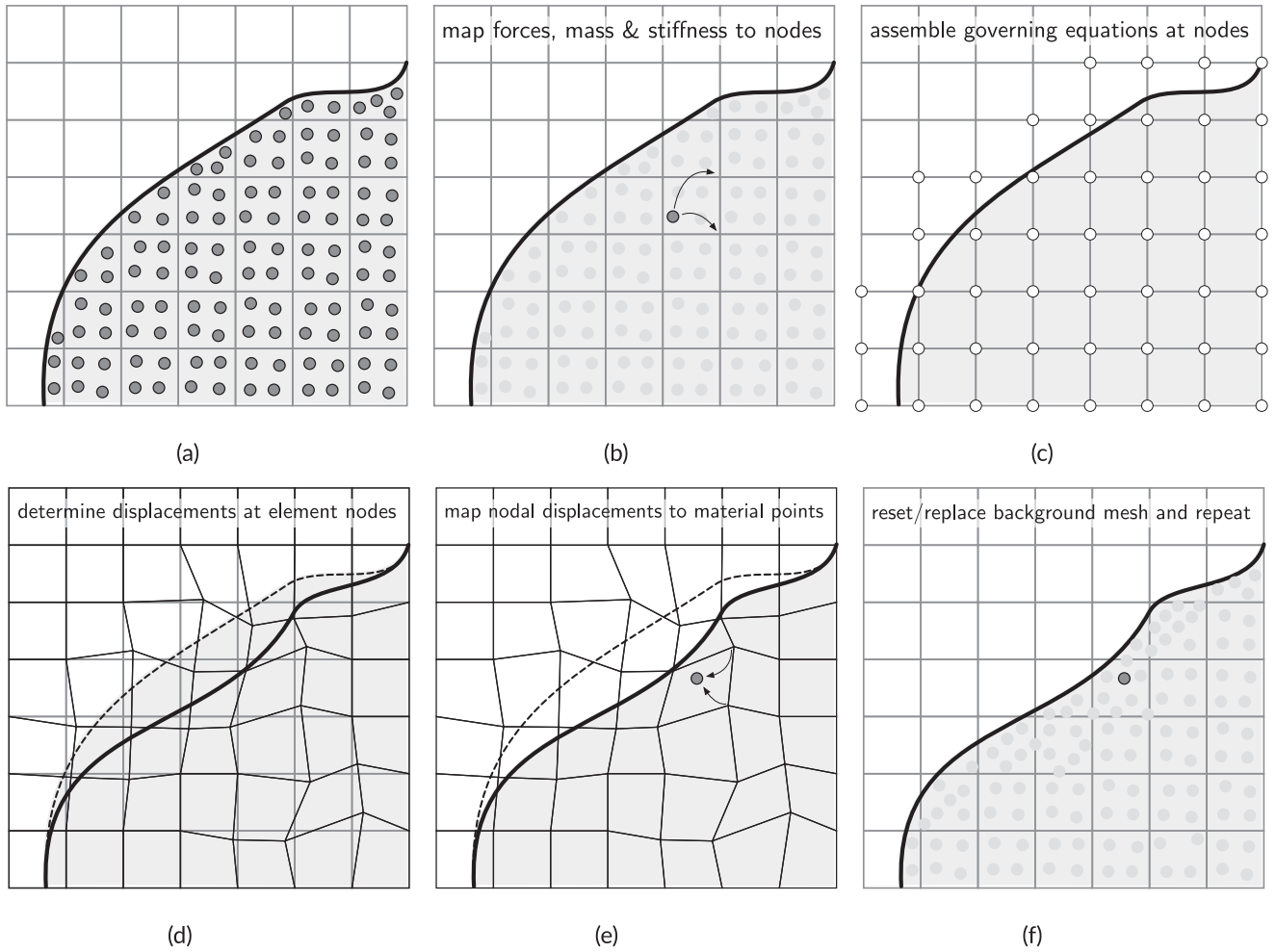


FIGURE 1 | Material point method steps (adapted from Coombs and Augarde [13]). (a) initial position, (b) point-to-grid map, (c) assembly, (d) grid solution, (e) grid-to-point map, and (f) update points & reset grid.

procedure. This paper is focused on dynamic stress analysis of solid materials, with an implicit Newmark time discretization. Key aspects of the formulation are provided in the following sections. These sections are deliberately brief, with specific references for full details, as the focus of the paper is on a new three-dimensional contact approach.

2.1 | Continuum Formulation

The continuum formulation adopted in this paper is the same as the quasi-static open-source AMPLE (A Material Point Learning Environment) code [13], but with the addition of inertia effects. Full details of the large deformation elasto-plastic continuum mechanics formulation used in this paper can be found in Charlton et al. [14] and Coombs and Augarde [13]. Within this approach, the deformation gradient is multiplicatively decomposed into elastic and plastic components and combined with a linear relationship between Kirchhoff stress and logarithmic elastic strain, along with an exponential map of the plastic flow rule. The combination of these ingredients allows isotropic small-strain plasticity algorithms to be used directly within a large-deformation setting, without modifying the stress update procedure [15]. The approach is widely used in large deformation

finite element methods (see, e.g., de Souza Neto et al. [16]), and in material point methods [1, 13, 14, 17–20].

2.2 | Material Point and Background Grid Spatial Discretization

A background grid of finite elements, K , allows the weak statement of equilibrium to be expressed as

$$\int_{\varphi_t(K)} [\nabla_x S_v]^T \{\sigma\} dV - \int_{\varphi_t(K)} [S_v]^T \{b\} dV + \int_{\varphi_t(K)} \rho [S_v]^T \{\dot{v}\} dV - \int_{\varphi_t(\partial\Omega)} \left(\{F_{N,v}^{\partial\Omega}\} + \{F_{T,v}^{\partial\Omega}\} \right) ds = \{0\} \quad (1)$$

where $\{\dot{v}\}$ and φ_t are the acceleration and motion of the material within the element, which is subjected to body forces, $\{b\}$, acting over its volume, V , with density, ρ , that generates a Cauchy stress, $\{\sigma\}$, in the element. $[S_v]$ contains the basis functions that map information from the nodes (or vertices, v) of the background grid to other locations within the grid. $[\nabla_x S_v]$ is the strain-displacement matrix containing derivatives of the basis functions with respect to the updated coordinates. The last term is the traction comprising the normal and tangential contact forces

for the deformable body, respectively $\{F_{N,v}^{\partial\Omega}\}$ and $\{F_{T,v}^{\partial\Omega}\}$. Note that the traction term is integrated over the boundary of the physical body, $\partial\Omega$, as in general the domain boundary will not coincide with the background mesh.

In the MPM, the physical body being analyzed is represented by a number of discrete material points with an associated volume, V_p , and mass, m_p . This allows the volumetric integrals in Equation (1) to be approximated by an assembly over the material points

$$\begin{aligned} & \mathbf{A}_{\forall p} ([\nabla_x S_{vp}]^T \{\sigma_p\} V_p - [S_{vp}]^T \{b\} V_p + [S_{vp}]^T \{\dot{v}_p\} m_p) \\ & - \mathbf{A}_{p \in P_c} (\{F_{N,vp}^{\partial\Omega}\} + \{F_{T,vp}^{\partial\Omega}\}) = \{0\} \end{aligned} \quad (2)$$

Note that the subscripts on the basis functions, $[S_{vp}]$, have changed to highlight that they depend on both basis functions associated with the background grid and the characteristic function associated with the material point, p , which describes a material point's *influence* (see Section 2.3 for details). The subscripts of the contact forces, $\{F_{N,vp}^{\partial\Omega}\}$ and $\{F_{T,vp}^{\partial\Omega}\}$, have also changed to highlight that contact is occurring at the material point $p \in P_c$, where P_c is the set of material points in contact with the rigid body. In this paper, it is assumed that Dirichlet boundary conditions are imposed directly on the nodes of the background grid as the imposition of general Dirichlet constraints is a separate area of research (see, e.g., [18, 21–23]). The traction term will be discretized in Section 4.

2.3 | Basis Functions

In this paper we adopt Generalized Interpolation Material Point (GIMP [10]), basis functions to mitigate the widely documented cell crossing instability and also to provide a convenient way to track contact between the deformable material (represented by material points) and a rigid body. The basis functions, S_{vp} , are obtained by integrating the product of the shape functions associated with the background grid, S_v , with a characteristic function, χ_p , over the cuboid defining the domain associated with the material point, Ω_p , normalized by the volume of the domain. This generates C^1 continuous basis functions that smooth the transfer of internal force from the material points to the grid nodes as a material point transitions between elements. The domain updating procedure is detailed in Section 5.2.

2.4 | Discretization in Time

The discrete weak statement of equilibrium (2) is discretized in time by a Newmark time integration scheme. The Newmark parameters are taken to be $\gamma = 1/2$ and $\beta = 1/4$, resulting in an unconditionally stable implicit algorithm for linear problems [24]. A key point within MPMs is that the nodal displacements at the end of each time step are discarded, and the background grid is reset or replaced. Therefore, it is assumed that the nodal displacements at the start of the step are zero, $\{u_v^n\} = \{0\}$, whereas the nodal velocities and accelerations at the start of the time step are projected from the material point values using

$$\{v_v^n\} = [M]^{-1} \mathbf{A}_{\forall p} ([S_{vp}]^T \{v_p^n\} m_p) \quad \text{and} \quad \{\dot{v}_v^n\} = [M]^{-1} \mathbf{A}_{\forall p} ([S_{vp}]^T \{\dot{v}_p^n\} m_p) \quad (3)$$

where $[M] = \mathbf{A}_{\forall p} ([S_{vp}]^T [S_{vp}] m_p)$ is the consistent mass matrix. $\{v_p^n\}$ and $\{\dot{v}_p^n\}$ at the material point velocities and accelerations at the start of the time step (assumed to be equal to those from the end of the previous time step). At the end of the time step, a FLIP grid-to-particle mapping is performed [25].

2.5 | Stabilization

The MPM can suffer from instabilities linked to the arbitrary nature of the interaction between the material points and the background grid, potentially leading to very small contributions to the mass and/or stiffness matrix. These small contributions can result in conditioning issues and, therefore, issues with the inversion of the mass/stiffness matrix. In this paper, the ghost penalty approach of Burman [26] is adopted to mitigate this issue based on the MPM implementation of Coombs [27]. The technique adds a penalty stabilization term to the mass and/or stiffness matrix that introduces additional continuity of the gradient of the solution across faces of the background grid at the boundary of the physical body (i.e., in elements with a small cut potential). In this paper the mass and stiffness stabilization parameters are set to $\gamma_M = \rho/4$ and $\gamma_K = E/30$, respectively, where ρ and E are the volume weighted average density and Young's modulus of the material points that occupy the elements that share the element boundary where the stabilization is applied.

3 | Rigid Body

To describe the contact kinematics between the rigid body and the material points, it is necessary to define the various coordinate systems that exist. This includes the local coordinates of the triangular facets that form the rigid body's surface, and also the global coordinates of the rigid body, which are used to describe its kinematics. Much of the details presented here can be found in the book by Wriggers [12]. However, the mathematical tools that are used here are briefly detailed for both readability and consistent nomenclature.

3.1 | Coordinate Systems

The surface of the rigid body is discretized by a triangular mesh, as in the left of Figure 2.

On each triangle in the global domain, K , a contravariant coordinate system is defined, $\mathbf{x}' = \mathbf{e}_\alpha \xi^\alpha$, where $\mathbf{x}' \in K$, is shown by the square marker in Figure 2. Similarly on the local domain \hat{K} , shown on the right Figure 2, another contravariant coordinate system is defined, $\boldsymbol{\eta} = \hat{\mathbf{e}}_\alpha \xi^\alpha$. Between the two coordinate systems, there is the affine mapping,

$$\mathbf{x}' = \Xi(\mathbf{x}_n, \boldsymbol{\eta}) \quad (4)$$

where \mathbf{x}_n are the nodal positions of the rigid body triangle. The mapping is such that the contravariant components, ξ^α , are connected between the coordinate systems [28],

$$\mathbf{x}' = \mathbf{e}_\alpha \xi^\alpha \quad \text{and} \quad \boldsymbol{\eta} = \hat{\mathbf{e}}_\alpha \xi^\alpha \quad (5)$$

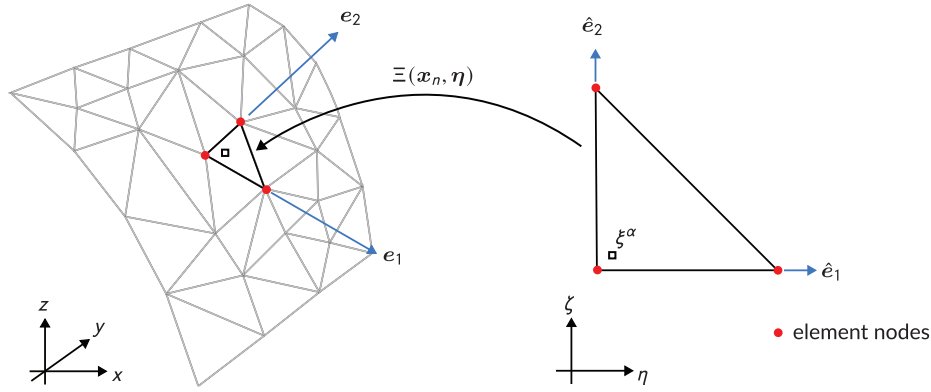


FIGURE 2 | The rigid body global and local coordinate systems.

such that the value ξ^α remains constant between the local and global domains when the mapping (4) is performed. To track the movement of a contact point over a triangle, it is convenient to do so with nodal shape functions and the local coordinates ξ^α defined at the nodes ξ_n^α , where n is the nodal number. The value of ξ^α can therefore be described as

$$\xi^\alpha = \sum_n^3 N_n(\xi) \xi_n^\alpha \quad (6)$$

where $N_n(\xi)$ are the nodal shape functions. Substituting Equation (6) into Equation (5) gives the description for the position \mathbf{x}' but using the local element shape functions,

$$\mathbf{x}' = \mathbf{e}_\alpha \sum_n^3 N_n(\xi) \xi_n^\alpha = \sum_n^3 N_n(\xi) \mathbf{x}_n \quad (7)$$

where \mathbf{x}_n is the position of the triangle corners in the global domain. Additionally, the tangent to the rigid body in the global domain \mathbf{t}_α , see Pietrzak and Curnier [29], is found with the derivative of shape functions with respect to ξ^α

$$\mathbf{t}_\alpha = \frac{\partial \mathbf{x}}{\partial \xi^\alpha} = \mathbf{e}_\beta \sum_n^3 \frac{\partial N_n(\xi)}{\partial \xi^\alpha} \xi_n^\beta = \sum_n^3 \frac{\partial N_n(\xi)}{\partial \xi^\alpha} \mathbf{x}_n \quad (8)$$

3.2 | Kinematics

A rigid body is defined by a set of nodes unable to move relative to each other; the motion of all the nodes is described with a single set of rigid body degrees of freedom. The work presented here was originally developed for geotechnical engineering problems, which often involve a chain or wire pulling a rigid body, such as a plough or anchor. Here, a truss frame is used to model the chain/wire, and the frame is also used to describe the kinematics of the rigid body. The kinematic description is achieved by using the vertices of a truss element to describe the position of all nodes. An example of this for a single triangle of the rigid body is shown in Figure 3, where the motion of the truss frame is restricted to the y -plane.

The truss element in Figure 3 is comprised of two nodes, \mathbf{x}_M and \mathbf{x}_D from which a tangent \mathbf{t}_{RB} and normal \mathbf{n}_{RB} are defined. They

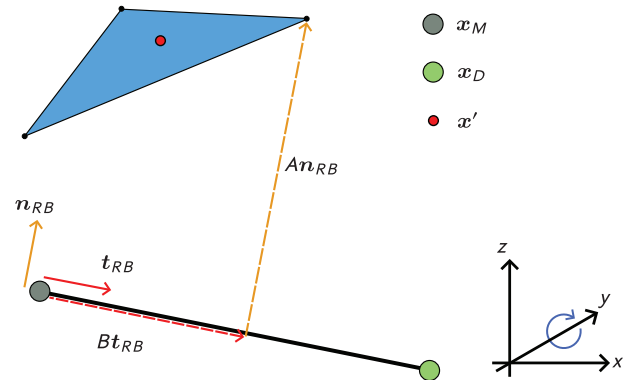


FIGURE 3 | Rigid body: Truss frame description.

are respectively computed by

$$\mathbf{t}_{RB} = \frac{\mathbf{x}_D - \mathbf{x}_M}{\|\mathbf{x}_D - \mathbf{x}_M\|} \quad \text{and} \quad \mathbf{n}_{RB} = \mathbf{R} \cdot \mathbf{t}_{RB} \quad (9)$$

where \mathbf{R} is a rotation matrix of 90° about the y -axis. The nodal position of the triangle element, \mathbf{x}_n , can now be described as function of \mathbf{x}_M , \mathbf{t}_{RB} , \mathbf{n}_{RB} and two scalar values B_n and A_n which have unique, and constant, values for each node,

$$\mathbf{x}_n = A_n \mathbf{I} \cdot \mathbf{n}_{RB} + B_n \mathbf{I} \cdot \mathbf{t}_{RB} + \mathbf{x}_M = (A_n \mathbf{R} + B_n \mathbf{I}) \cdot \mathbf{t}_{RB} + \mathbf{x}_M = \mathbf{G}_n(\theta) \quad (10)$$

where \mathbf{I} is the identity matrix and $\mathbf{G}_n(\theta)$ is the function for the position \mathbf{x}_n dependent on the variable θ which is a vector containing the points \mathbf{x}_M and \mathbf{x}_D . Every node in the rigid body is described by Equation (10) which for all nodes has the variables \mathbf{x}_M and \mathbf{x}_D , hence there is potential for relative motion between the nodes. Substituting Equation (10) into (7) gives,

$$\mathbf{x}' = \sum_n^3 N_n(\xi) [(A_n \mathbf{R} + B_n \mathbf{I}) \cdot \mathbf{t}_{RB} + \mathbf{x}_M] = \sum_n^3 N_n(\xi) \mathbf{G}_n(\theta) \quad (11)$$

In Section 4, \mathbf{x}' is used as the contact point of the rigid body with the material point, for which the implicit solver will require its first and second variations, provided in Appendix A.

Lastly, the residual for the equation of linear momentum of the truss frame, with the contact forces, is included in the monolithic solver, presented in Section 2.4, to form a coupled problem. The residual for linear momentum takes the form,

$$\begin{aligned} & \mathbf{A}_{f \in F} \{\sigma_f\} dV - \mathbf{A}_{f \in F} \{b\} dV + \mathbf{A}_{f \in F} [m_f] \{\dot{v}_f\} dV \\ & - \mathbf{A}_{l \in L} (\{F_N^l\} + \{F_T^l\}) ds = \{0\} \end{aligned} \quad (12)$$

where $\{\sigma_f\}$ is the internal truss force, F is the set for all truss elements f , L is the set for all rigid body triangles l , $[m]$ is the nodal mass matrix for f , $\{b_f\}$ is the nodal external force vector, $\{\dot{v}_f\}$ is the nodal acceleration and the last term is the contact forces acting on the triangles of the rigid body, split into normal, $\{F_N^l\}$ and tangential components $\{F_T^l\}$, [30].

4 | Contact

This section presents the description of the contact forces present in Equations (2) and (12). When considering the contact between the material point p and the triangle l , the general form for the contact forces is

$$\begin{aligned} \delta U &= \delta U_N + \delta U_T = \int_{\psi_l(l) \cap \delta(\mathbf{x}')} (\{F_N^l\} + \{F_{N,vp}^{\partial\Omega}\}) d\mathbf{s} \\ &+ \int_{\psi_l(l) \cap \delta(\mathbf{x}')} (\{F_T^l\} + \{F_{T,vp}^{\partial\Omega}\}) d\mathbf{s} \end{aligned} \quad (13)$$

where $\delta(\mathbf{x}')$ is the Dirac delta function and \mathbf{x}' is the projection of the position of the material point p onto the rigid body surface, using the Closest Point Projection (CPP) scheme, detailed in Section 4.2.

4.1 | Contact Introduction

This section describes the contact formulation between the rigid body and the GIMPs. Using the same contact methods as in the Finite Element Method (FEM), the contact formulation and methodology are driven by the gap function [12, 31]. The gap function is the projection of a point from the secondary surface (s), with coordinates \mathbf{x}' , onto the main surface (m), with coordinates \mathbf{x} . The gap function is used to: (i) determine if there is contact and between which point and surface; (ii) how much overlap there is; and (iii) through the rate derivative of the gap function to determine the relative tangential velocity.

Here, the CPP scheme is used to determine the gap function, see the works of Curnier and their coworkers [29, 31]. However, other methods do exist, such as ray-tracing (see Poullos and Renard [32]), which has been applied to GIMP-to-GIMP contact, Pretti [6].

4.2 | Gap Function

To define the gap function, first the definition of the main (m) and secondary (s) surfaces/domains needs to be established, as well as the general contact methodology. Here, a point-to-surface contact

is used, where the points are the primary domain, consisting of the GIMP vertices, and the secondary domain is the triangular surface of the rigid body.

The CPP gap function is the minimum distance of a point's projection point onto the surface, defined as,

$$\begin{aligned} \mathbf{g}_N(\xi(\tau)^\alpha, \tau) &= g_N(\xi(\tau)^\alpha, \tau) \mathbf{n}(\xi(\tau)^\alpha, \tau) \\ &= \mathbf{x}(\tau) - \mathbf{x}'(\xi(\tau)^\alpha, \tau) \quad \text{and} \quad g_N = \mathbf{g}_N \cdot \mathbf{n} \end{aligned} \quad (14)$$

where τ is time and $\xi(\tau)^\alpha$ is a function that describes the local location of the projection on the surface. The normal contact law is described by the Signorini–Hertz–Moreau conditions, which are a function of g_N and the corresponding normal penetration force p_N ,

$$g_N \begin{cases} = 0 & \text{contact} \\ \geq 0 & \text{no contact} \end{cases}, \quad p_N \begin{cases} \leq 0 & \text{contact} \\ = 0 & \text{no contact} \end{cases} \quad \text{and} \quad g_N p_N = 0 \quad (15)$$

Where the last condition is relaxed for the penalty method.

Following the work of Curnier et al. [31] an objective definition of the relative velocities can be obtained as a total time derivative of \mathbf{g}_N , which is necessary to evaluate the frictional component of contact. It is expressed as

$$\begin{aligned} \dot{\mathbf{g}}_N(\xi^\alpha(\tau), \tau) &= \dot{g}_N(\xi^\alpha(\tau), \tau) \mathbf{n}(\xi^\alpha(\tau), \tau) + g_N(\xi^\alpha(\tau), \tau) \dot{\mathbf{n}}(\xi^\alpha(\tau), \tau) \\ &:= \dot{\mathbf{g}}_N(\xi^\alpha(\tau), \tau) + \dot{\mathbf{g}}_T(\xi^\alpha(\tau), \tau) \\ &:= \dot{\mathbf{g}}_N(\xi^\alpha(\tau), \tau) + \mathbf{t}_\alpha(\xi^\alpha(\tau), \tau) \dot{\xi}^\alpha(\tau) \end{aligned} \quad (16)$$

where $\dot{\mathbf{g}}_N$ is rate of penetration and $\dot{\mathbf{g}}_T$ is the relative tangential velocity between the two points. Following the work of [12, 31] the residual for contact can be expressed as

$$\delta U = \underbrace{\int_{\psi_l(l) \cap \delta(\mathbf{x}')} (\delta g_N p_N) d\mathbf{x}}_{\text{normal}} + \underbrace{\int_{\psi_l(l) \cap \delta(\mathbf{x}')} (\delta \xi^\alpha \mathbf{t}_\alpha \cdot \mathbf{p}_l) d\mathbf{x}}_{\text{tangential}} \quad (17)$$

where $\delta(\mathbf{x}')$ is the Dirac delta function at the current position of the secondary surface. Additionally, the first variations of the normal and tangential gap rates are required $\dot{\mathbf{g}}_N = \mathbf{n} \delta g_N$ and $\dot{\mathbf{g}}_T = \mathbf{t}_\alpha \delta \xi^\alpha$. The linearization of Equation (17) for the normal and tangential components is respectively found in Appendix B.

4.3 | Normal and Tangential Contact Forces

The magnitude of the normal force, in the direction \mathbf{n} , to resist interpenetration, p_N in Equation (17), is calculated using a penalty force

$$p_N = c_N g_N \quad (18)$$

The methodology presented here for determining the friction acting between the two bodies is an extension of the 2D method proposed by Bird et al. [1] for GIMP-to-rigid body contact, which itself is based on the work of Wriggers [12]. The methodology starts by defining the total tangential movement of a point on the surface,

$$\mathbf{g}_T = \int_{\tau} \dot{\mathbf{g}}_T dt = \int_{\tau} \dot{\mathbf{g}}_{\text{slip}} dt + \int_{\tau} \dot{\mathbf{g}}_{\text{stick}} dt = \mathbf{g}_{\text{slip}} + \mathbf{g}_{\text{stick}} \quad (19)$$

which is comprised of the components: (i) \mathbf{g}_{slip} , which is the purely dissipative and forms the plasticity component of the friction model, and (ii) the tangential stick, $\mathbf{g}_{\text{stick}}$. Here, the Coulomb friction law is used, where the frictional force is defined as,

$$\mathbf{p}_T = \mu |p_N| \frac{\dot{\mathbf{g}}_{\text{slip}}}{\|\dot{\mathbf{g}}_{\text{slip}}\|} \quad \text{if } \|\mathbf{p}_{\text{stick}}\| > \mu |p_N|, \quad \text{where } \mathbf{p}_{\text{stick}} = \epsilon_T \mathbf{g}_{\text{stick}} \quad (20)$$

where μ is the coefficient of friction, which is assumed constant, and ϵ_T is a penalty constant. $\mathbf{p}_{\text{stick}}$ is a penalty method to enforce sticking contact; it is a purely elastic and recoverable motion of the particle along the surface. The friction law is subject to the Karush-Kuhn-Tucker (KKT) conditions,

$$f = \|\mathbf{p}_{\text{stick}}\| - \mu |p_N| \leq 0, \quad \lambda \geq 0 \quad \text{and} \quad f\lambda = 0 \quad (21)$$

where f is the frictional yield function, and λ is the yield rate. The computation and the linearization of frictional contact are presented in Appendix B.

5 | Numerical Implementation

This section details two critical elements of the material point-rigid body interaction that need careful treatment to realise an accurate and robust numerical implementation, namely: (i) the contact detection approach using the corners of the GIMP domains and (ii) the update of these domains to maintain a stable, energy consistent solution.

5.1 | Closest Point Projection (CPP) for Contact Detection

The description of the gap function is fundamental to modeling contact, as described in Section 4. However, when considering contact between a point and an irregular surface there are algorithmic nuances that need to be discussed which can be overlooked when going from a mathematical-to-algorithmic description, particularly in the case when GIMP domains are used to detect contact. The focus of this section is the calculation of Equation (14) and presents an extension of the 2D contact methodology presented by Bird et al. [1] to 3D.

The vertices of the GIMP domains are the points in contact with the faceted surface of the rigid body, consistent with the point-to-surface contact described in Section 4. This is necessary so that contact occurs on the material boundary, otherwise the contact is not consistent and spurious stresses are observed for the contact GIMPs [1]. The GIMP domains provide an explicit representation of the extent of the physical material that is consistent with the discretisation of the governing equations. The integration to construct the basis functions, \mathcal{S}_{vp} , is exact; thus, through inspection of the calculation of the linear momentum residual, (2), it is also an integral of a function over an exact domain. The point-to-surface contact between a vertex of the GIMP and a

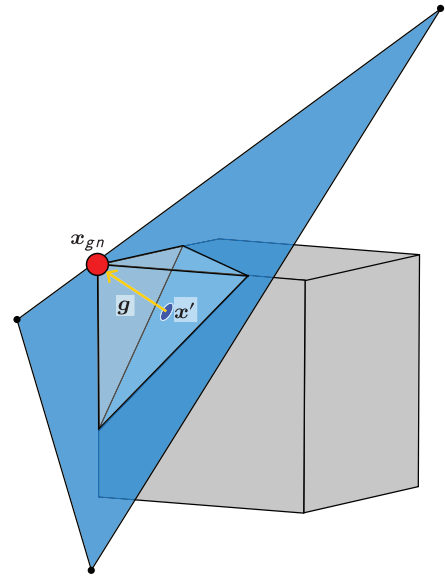


FIGURE 4 | CPP: A contact vertex (red dot) of a GIMP domain, shown in gray, in contact with a rigid body triangle, blue. The gap function is also shown by the yellow arrow.

triangle of the rigid body surface is described with Figure 4 where, the position of the GIMP vertex is described as

$$\mathbf{x}_{gn} = \sum_{v \in E} N_v \mathbf{x}_v \quad (22)$$

which when in contact is the point \mathbf{x} that is projected onto point \mathbf{x}' in Equation (14).

As described in Section 3, the surface of the rigid body is constructed from a triangular mesh to produce a constant normal direction over each triangle surface. Points and lines of the mesh do not have a normal description and hence it is not possible to define a gap function for them, see the work of Curnier et al. [31] for this argument. Hence, contact is only observed on the triangle faces.

The choices made so far can have two possible issues when considering rigid bodies with concave surface representations that, if not properly addressed, could undermine the contact formulation. These issues are associated with the governing equilibrium equation (specifically, the contact detection and associated forces) and the convergence of the iterative solver. In terms of contact forces, an issue with not being able to define a gap function for the points/lines is that it may be possible for points to travel into the domain undetected in the case of concave edges/corners (contact detection blind spots). However this problem is mitigated by each GIMP having 8 potential points of contact, and in addition CAD software can be used to chamfer concave edges/corners to reduce the likelihood of this phenomenon occurring. A concave 3D scenario where contact is not detected at some GIMP corners is shown in Figure 5a, with a 2D slice shown in Figure 5b. The green and red regions are where the contact constraint can and cannot be applied, respectively. From an algorithmic point of view, these red/green zones are not identified explicitly; the red regions are simply the result of the CPP being onto a line or point, and the green regions are a CPP onto a

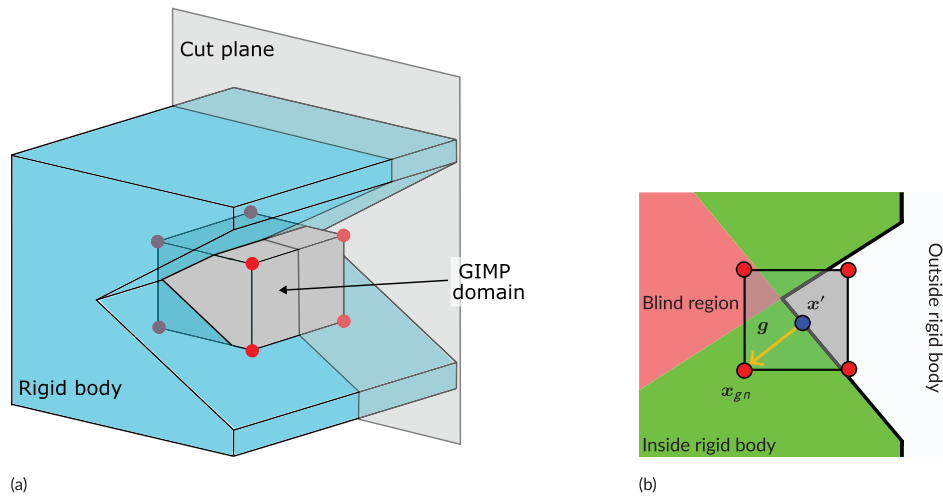


FIGURE 5 | Closest point projection: (a) is the 3D view of a GIMP in contact with a concave edge of the rigid body, (b) is the corresponding slice view through the domain with green regions showing where the CPP is onto triangles, and red regions the CPP onto points/lines of the rigid body.

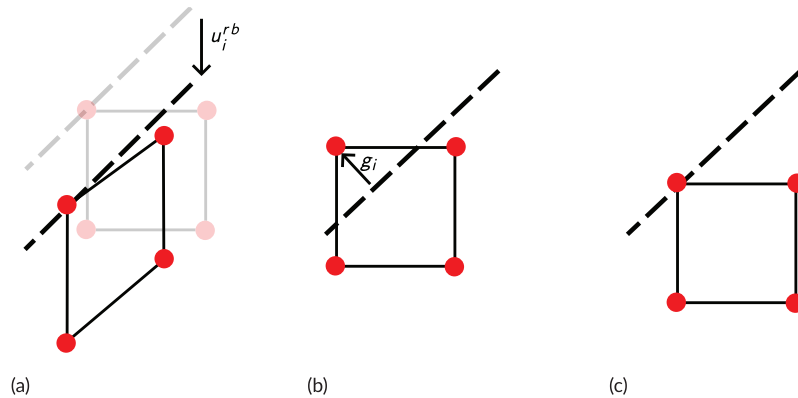


FIGURE 6 | GIMP contact update: The converged position of the GIMP domain for time step n is shown in (a), the updated position for the beginning of step $n+1$ is shown in (b) and the updated position for the beginning of step $n+1$ after the gap minimization in (c). The surface of the rigid body is shown by the dashed line.

triangle. This represents a potential source of numerical instability for concave rigid body geometries. A point in the red region could be quite far inside the rigid body since there is no force resisting the penetration. During the load step this point could move into green region with a significant gap size, resulting in a large instantaneous contact force that could cause convergence problems¹. To ensure convergence with a reasonable step size, once a GIMP vertex enters the red region its normal penalty is set to zero, is deemed inactive, and its contribution remains zero throughout the remainder of the time step. This is similar to the active-inactive set methods presented in other works [33]. In this class of methods, a check is performed to ensure the active set is *optimal* in terms of a compromise between enforcing the contact conditions and stability of the non-linear solution process. Here, the possible set of contact points can only be reduced during the load step and is therefore termed a no-return active set strategy. The decision to not perform additional checks is influenced by various mitigating factors, primarily that the density of the contact detection points, the GIMP vertices, is higher than the density of the nodes of the background grid. If a GIMP has all its vertices set to a zero penalty parameter, nearby GIMPs are likely to be in contact. This means that the contribution of a single

inactive vertex to the contact force assembled on the grid is likely to be small. It also means that the case of a single vertex becoming inactive should not significantly influence the behavior of the Newton-Raphson solver. Furthermore each GIMP has eight vertices, any of which could be in contact with the rigid body. The likelihood of all these vertices being set to an inactive state when they should be in contact during a time step is small.

5.2 | GIMP Domain Update Procedure

Large time steps can be taken when solving a contact problem implicitly, and in the GIMPs which are in contact can undergo significant deformation, as shown in Figure 6a, during which the normal contact condition remains met. Once the time step is complete a reset algorithm is performed on the mesh and GIMP domains, see Figure 1f, during which the GIMPs are reset from a distorted to regular shape, with the volume of the GIMP domain equal to the material volume, see Figure 6b. Whilst this is acceptable in other regions of the mesh, for GIMPs in contact a large, purely numerical, increase in the gap function is introduced, as shown in Figure 6b, despite no external work being performed.

ALGORITHM 1 | Energy Minimization Algorithm.

```

Calculate  $E^{\text{old}} = \sum_n \left( \epsilon_{N,n}^{\text{old}} g_{N,n}^{\text{old}} \right)^2$ ;
exit  $\leftarrow 0$ ;
while exit = 0 do
    Calculate the residual  $R_i = \frac{\partial E}{\partial x_i}$ ;
    if  $E/E^{\text{old}} > 0.01$  then
        Calculate update step vector  $v_i = \frac{R_i h_p}{200 |R_i|}$ ;
        Update the MP position  $x_i \leftarrow x_i - v_i$ ;
        Recalculate  $E$ ;
    else
        exit  $\leftarrow 1$ ;
    end
end

```

The result is that at the beginning of the new time step, a significant unrealistic normal contact force can exist. This affects the numerical stability of the algorithm since a large nonlinearity is introduced, which often results in non-convergence of the solver. This overlap is particularly problematic since the size of the nonlinearity is the same, regardless of the size of the time step. Therefore, reducing the time step size and corresponding load increment size can restore stability, but the solver will continue to fail regardless of the time step size; consequently, the simulation will fail.

To solve this problem an energy minimization is performed during the update of the GIMP. The energy minimization is presented as,

$$\underset{x_i \in \mathcal{R}^3}{\operatorname{argmin}} E(x_i) \quad \text{where} \quad E(x_i) = \sum_n \left[\epsilon_{N,n}^{\text{old}} g_{N,n}^{\text{old}} - \epsilon_{N,n}^{\text{new}} g_{N,n}^{\text{new}}(x_i) \right]^2 \quad (23)$$

where x_i is the position of the GIMP domain centre, $g_{N,n}$ is the magnitude of the normal gap function at node n , $\epsilon_{N,n}$ is the normal penalty, with the superscripts *old* and *new* corresponding to the previously converged and current variable state. The authors emphasise that this is a solution to the problem, but there could be other possible variations on this, perhaps also considering how much the material is moved to satisfy (23). However, for the range of problems considered here, using (23) has delivered both stable and accurate results.

The method to solve this problem is presented in Algorithm 1. This will update the GIMP position from its uncorrected state, Figure 6b, to its new state, Figure 6c. For this algorithm, an explicit forward Euler method was used. An implicit method was considered, however during numerical testing it was observed that during the solve it moved the GIMP so it was out of contact, meaning $g_{N,n}^{\text{new}} = 0 \forall n$ causing the convergence of Algorithm 1 to stagnate. In this regard the forward Euler approach was considered more robust, with the step size of the method constrained by the minimum side length, h_p , of the GIMP in contact, divided by 200.

The factor of $h_p/200$ was chosen as a compromise, as the algorithm is entirely multiplicative and fast; however, reducing

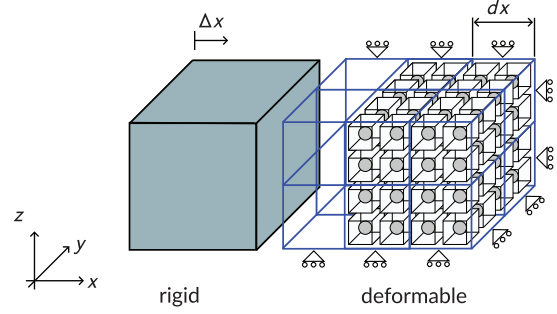


FIGURE 7 | Cube under compression: The initial geometry and mesh setup.

the step size beyond a reasonable value could make it expensive. $h_p/200$ is also an upper bound to ensure the algorithm converges and to limit the possibility of the GIMP being pushed out contact.

6 | Numerical Simulations

This section will demonstrate the capabilities of the proposed method via four numerical examples. The first two examples test the method against analytical solutions to check specific aspects of the contact formulation. The third and fourth examples are comparisons with physical modeling results to demonstrate that the method can obtain robust, physically correct results without parameter tuning.

6.1 | Cube Under Compression

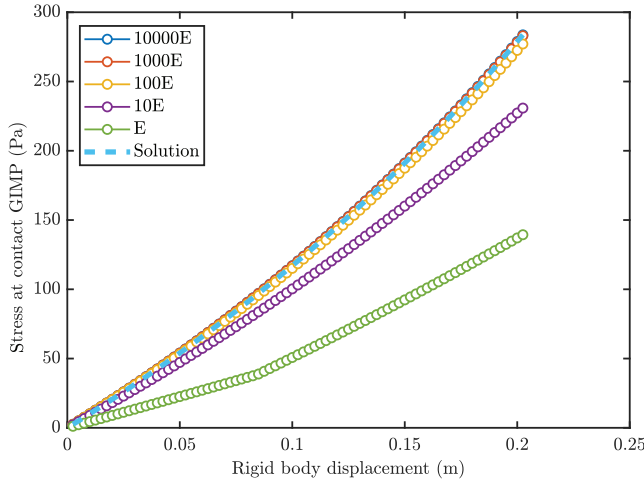
6.1.1 | Example Scope

A 1D contact problem with an analytical solution, but modeled in 3D, is used as a patch test for the normal contact formulation. The patch test will investigate the stress solution of one of the GIMPs in contact with the rigid body, as an inconsistent formulation will show poor agreement with the analytical solution [34]. Also considered is the stress solution and the global error when the normal contact penalty is varied. In the limit as the penalty $\rightarrow \infty$ the error in the Signorini–Hertz–Moreau conditions should tend to zero, and hence the stress solution converges to the true solution.

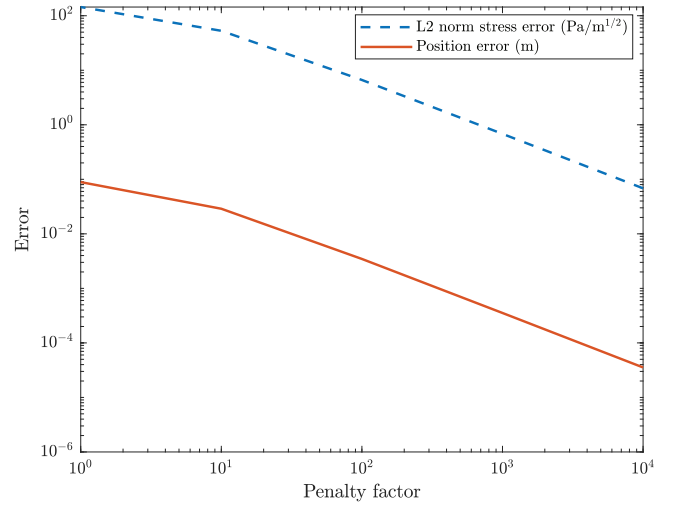
6.1.2 | Setup

The geometry of the problem is shown in Figure 7 and consists of two unit-sized cubes, one rigid and one deformable. The rigid body is displaced in the x -direction by Δx whilst the deformable body has roller boundary conditions on all mesh boundaries. As shown in Figure 7, the GIMP faces which will be in contact with the rigid body are not consistent with a mesh boundary, hence are free to move subject to the contact.

The deformable body is elastic with Young's Modulus $E = 10^3$ Pa, Poisson's ratio $\nu = 0$ and a contact normal penalty of $\epsilon_N = p_f E$ Pa, where p_f is the penalty factor that is used to vary the contact penalty. It is discretized uniformly with a Cartesian mesh with element edge length $dx = 0.1$ m. Each element initially contains 2 GIMPs in each direction with edge length $\frac{1}{2} dx$.



(a)



(b)

FIGURE 8 | Cube under compression: (a) is the stress at the contact GIMP for different penalty values, with the corresponding error for a rigid body displacement of 0.2 m shown in b.

Initially, the distance between the rigid and deformable body is 10^{-3} m, the rigid body is then displaced $\Delta z = -0.2001$ m over 5 time steps. The error in the L^2 norm is presented as

$$e = \left(\sum_p |\sigma - \sigma_p|^2 V_p^0 \right)^{1/2} \quad \text{with} \quad \sigma = E \log\left(\frac{l}{l_0}\right) \left(\frac{l_0}{l}\right) \quad (24)$$

as the analytical stress solution, which is constant, where l is the deformed length of the column, measured here using the final position of the rigid body contact surface, and l_0 is the original length of the deformable body with length 1m. V_p^0 the original volume of the GIMP, and σ_p is the stress at the GIMP.

6.1.3 | Results Discussion

The results presented here demonstrate that the stress at GIMPs in contact with the rigid body is consistent and converges to the analytical solution when the penalty is increased for a range of rigid body displacements, as shown in Figure 8a. The results indicate that when p_f is near $100E$, there is good agreement between the numerical and analytical results for this problem. Additionally, Figure 8b shows the global stress solution error and the position error, the interpenetration between the GIMP in contact and the rigid body. Both error measures decrease as the penalty factor increases. These figures therefore show that the stress solution for the GIMP in contact with the rigid body is consistent and that when the penalty is increased the overlap between the two bodies converges to zero.

6.2 | Rolling Sphere

6.2.1 | Example Scope

The previous problem demonstrated optimal convergence for a pseudo-static problem, which considered only normal contact.

Here, the normal and frictional contact formulation is validated by modeling a sphere rolling down a slope. The numerical results are compared to the problem's analytical solution for a range of friction coefficients, testing the numerical framework's ability to accurately capture the slip and stick states of Coulomb friction.

6.2.2 | Setup

Figure 9a shows the loading, geometry, and mesh for this problem. Although the problem models a sphere rolling down a 45° slope, the slope is represented as horizontal to ensure a smooth interface between the sphere and the GIMPs. If the slope was angled and gravity applied in the vertical direction, the slope, represented by the vertices of the GIMP domains, would not be smooth and there is the potential that the sphere could bounce depending on the exact interaction between the sphere and the domain corners at a given time step. The distance between the contact points would also be larger, which would likely give a less accurate result with oscillations in the rotational velocity. To simulate the angled slope, gravitational acceleration is applied at an angle corresponding to the original slope, with $g_i = 9.81 \times [1/\sqrt{2}, 0, -1/\sqrt{2}]^T$ m/s².

The kinematics of the rigid body are modeled by a series of elastic truss elements with only displacement degrees of freedom. Since the rigid body is free to rotate and translate, both the translational and rotational inertia need to be represented correctly. Although this is a 3D problem, the sphere is restrained in the y -direction and hence the rotational inertia needs only to be correct about the y -axis. Therefore, the truss elements are arranged as in Figure 9b. At the centre of the sphere is a node with zero mass, which is surrounded by a ring of equally spaced nodes on the y -plane, which do have mass. To ensure the rotational inertia of the ring is consistent with the sphere's rotational inertia, the diameter of the ring is set to $d_m = d_b \sqrt{(2/5)}$. Here, 100 nodes are used, each having a mass of $1/100$ kg.

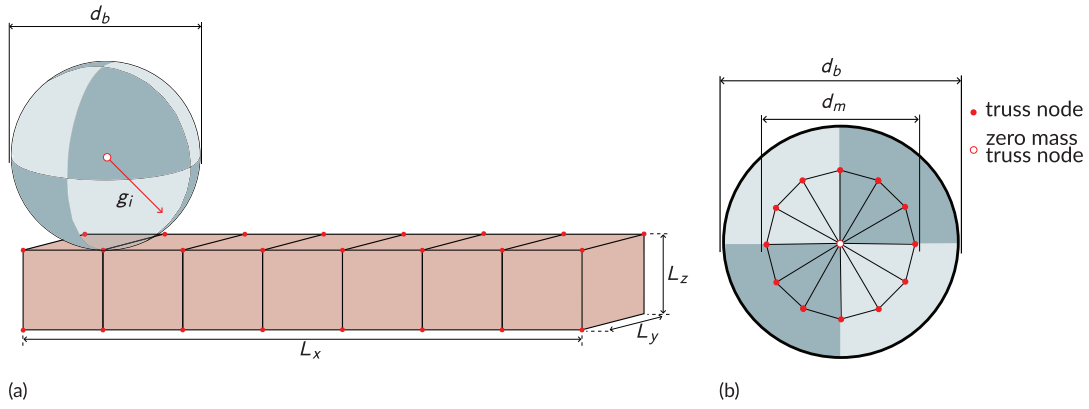


FIGURE 9 | Rolling sphere: Initial geometry and mesh setup is shown in (a) and the corresponding truss frame in (b).

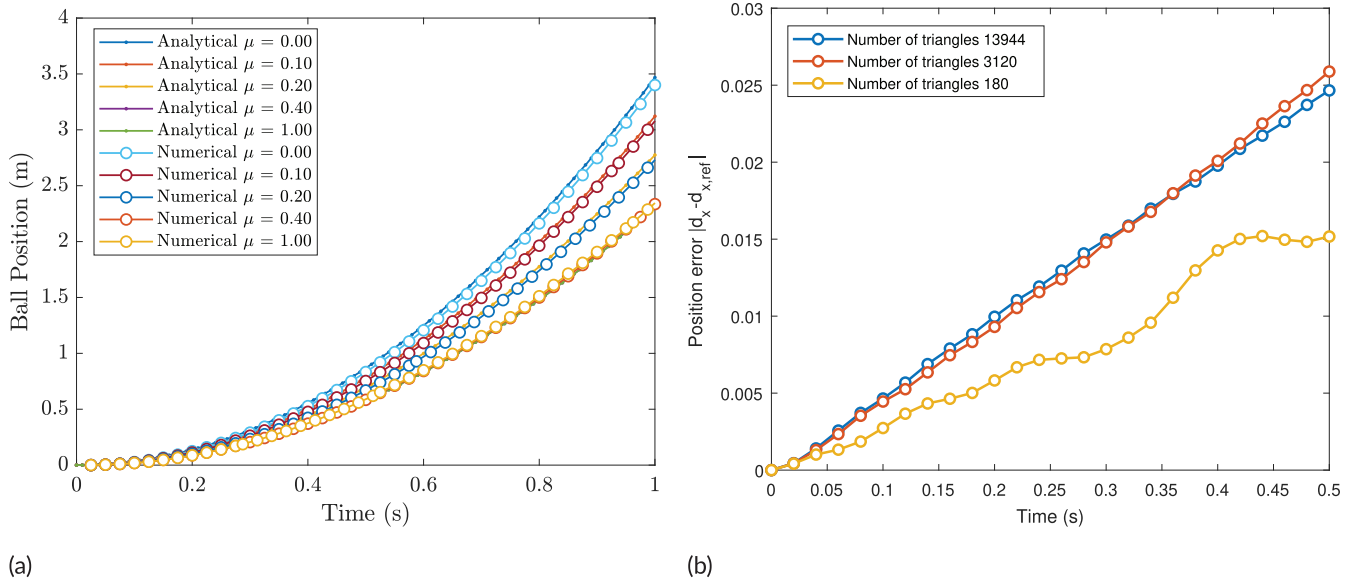


FIGURE 10 | Rolling sphere: The comparison of simulation results with reference data for different coefficients of friction is shown in (a), (b) considers different sphere refinements for $\mu = 0.2$.

The sphere has a diameter $d_b = 1$ m and is constructed from 3120 triangles arranged on a latitude-longitude grid. The level of refinement of the sphere was chosen as a compromise. Too few triangles and the sphere would bounce along the surface with all results tending to $\mu = 0.0$. Too many triangles would increase the cost of the simulation, but with little change to the results. The smallest and most slender triangles are at the poles, whilst the most regular and largest triangles are at the latitude 0° . The sphere is oriented in Figure 9a such that the equator of the sphere, where the most regular triangles exist, rolls along the material points. The material domain has dimensions, $L_x = 10$ m, $L_y = 1$ m, $L_z = 1$ m. The elements in the domain are of unit size and individually contain 4 material points in each direction. The analytical solution for this problem is defined for two rigid bodies in contact. For the deformable body to behave like a rigid body, homogeneous Dirichlet BCs were applied on all its exterior surfaces. The normal and tangential contact penalties for this problem are set as $50E$ and $25E$, with $E = 10^5$ Pa.

The analytical solution to this problem is presented as the distance d_x the sphere has moved down the slope as a function

of time. The solution has two forms, depending on whether the frictional contact is in a slip or stick state

$$d_x(t) = \begin{cases} (gt^2/2)[\sin(\theta_s) - \mu \cos(\theta_s)] & \text{if slipping, } \tan(\theta_s) > 3\mu \\ gt^2 \sin(\theta_s)/3 & \text{else sticking} \end{cases} \quad (25)$$

where $g = |g_i|$ is the gravitational acceleration, $\theta_s = 45^\circ$ is the slope angle, t is time and $\mu \in \{0, 0.1, 0.2, 0.4, 1.0\}$ are the friction coefficients considered here.

6.2.3 | Results Discussion

A comparison of the numerical and analytical results is shown in Figure 10a.

For $\mu \in \{0, 0.1, 0.2\}$, the sphere is in a slip state, with increasing μ , less slip occurs and hence the slower ball velocity. Over this range, Figure 10a shows good agreement, with the numerical results showing a very slight under-prediction of the ball

TABLE 1 | Rolling sphere: Comparison of relative sphere position at $t = 0.5$ s with $\mu = 0.2$ and varying tangential penalty parameter values against a reference solution of 0.6674 m, for $\epsilon_T = 2500E$.

Penalty parameter, ϵ_T	0.0025E	0.025E	0.25E	2.5E	25E	250E
Difference (%)	20.0	8.6	1.0	6.8×10^{-4}	0.0	0.0

TABLE 2 | Rolling sphere: Comparison of simulation time and position at $t = 0.5$ s with $\mu = 0.2$ for varying sphere discretization. The analytical solution is 0.6937 s.

Number of surface triangles	180	3120	8844	11 704	13 944
Run time (s)	44	276	560	1707	2587
Position (m)	0.6785	0.6674	0.6679	0.6677	0.6690
Position error (%)	2.19	3.79	3.72	3.74	3.56

position with time. Good agreement is also seen for the stick states, $\mu \in \{0.4, 1.0\}$, demonstrating that once the sphere is sticking, the solution is largely invariant to μ . Since there are GIMP vertices coming into contact at the front of the sphere, and leaving contact on the trailing surface, if a small time step is used, such as in an explicit analysis, high-frequency oscillations in the sphere's rotation velocity could manifest. However, high frequencies are not seen in the results presented here due to adopting an implicit time stepping algorithm with a time step of $dt = 0.02$ s. As discussed previously, low-frequency oscillations (i.e., bouncing) could occur if a coarse representation of the sphere is adopted; these oscillations are avoided by sufficiently refining the sphere's surface.

The tangential penalty parameter value influences the results in both slip and stick states. For slipping to occur, the trial tangential force needs to exceed a limiting value (see Equation (B12)). Lowering the tangential penalty allows more relative movement under a stick state, which represents a less rigorous enforcement of the KKT conditions. The impact of changing the tangential penalty parameter, ϵ_T , on the sphere position at $t = 0.5$ s with $\mu = 0.2$ is reported in Table 1, where the case of $\epsilon_T = 2500E$ is taken as the reference solution. Table 1 demonstrates that for the adopted normal penalty parameter, there is no change in the sphere's position vs. the reference case provided that $\epsilon_T \geq 25E$.

In the setup for this numerical experiment, a point was made that the number of surface triangles was a compromise between an accurate representation of the sphere's surface and the run time. Table 2 presents a comparison of the computational time with the sphere's position at $t = 0.5$ s for $\mu = 0.2$ for different numbers of surface triangles representing the sphere's surface. Table 2 shows that increasing the number of surface triangles from 3120 to 13 944 slightly improves the agreement between the numerical and analytical response, but at a 9.4 times run time increase. It can also be seen that the position of the sphere is relatively insensitive to the number of surface triangles between the 3120, 8844, and 11 704 discretizations. In this context, 3120 surface triangles represent a good compromise between accuracy and run time. Representing the sphere with 180 surface triangles appears to offer a more accurate result—this is an artefact and linked to the sphere acting more like a polyhedron with the coarse discretization, and by chance offering a better agreement with the analytical solution. This is confirmed by Figure 10b that shows

the position error-time response of the sphere with 180, 3120, and 13 944 surface triangles. The 180 case is oscillatory, linked to the sphere bouncing along the surface as relatively large triangular facets come in and out of contact. The other two discretizations show a monotonically increasing error with time, again with little difference between the 3120 and 13 944 cases.

6.3 | Cone Penetration Test

6.3.1 | Example Scope

In this section, a pseudo-static Cone Penetration Test (CPT) into dry sand with a homogeneous relative density is performed. The cone resistance, the vertical force acting on the cone, is then compared to experimental results obtained by Davidson et al. [35] for two different relative densities of sand, and a range of mesh refinements.

6.3.2 | Setup

The geometry and node distribution of the problem is shown in Figure 11a. Provided that the external boundaries are sufficiently far from the cone, the stress solution around the cone is symmetric in the circumferential direction. Problem symmetry could be exploited to reduce computational cost, as in the axisymmetric model of Bird et al. [1], however, in this case, one quarter of the problem is analyzed to test the 3D implementation. This is done by setting roller boundary conditions at $x = 0$ m and $y = 0$ m that represent planes of symmetry. On the remaining external boundaries, $x = L_x$ m, $y = L_y$ m, and $z = 0$ m, and roller boundary conditions are also applied. The cone's displacements are fully prescribed; in total, the CPT is displaced -5 m in the z -direction over 200 equal time steps, with equal load increment. However, if a time step fails, the step size is reduced by a factor of 2 until convergence is achieved. The step size is then reset to the original size, and the analysis progresses until the specified displacement is achieved.

The dimensions of the body are provided in Table 3. The red portion of the domain, shown in Figure 11a, is defined by the dimensions U_x , U_y , and U_z . In this region, the discretization is uniform with length dx . In the remainder of the domain, the blue region,

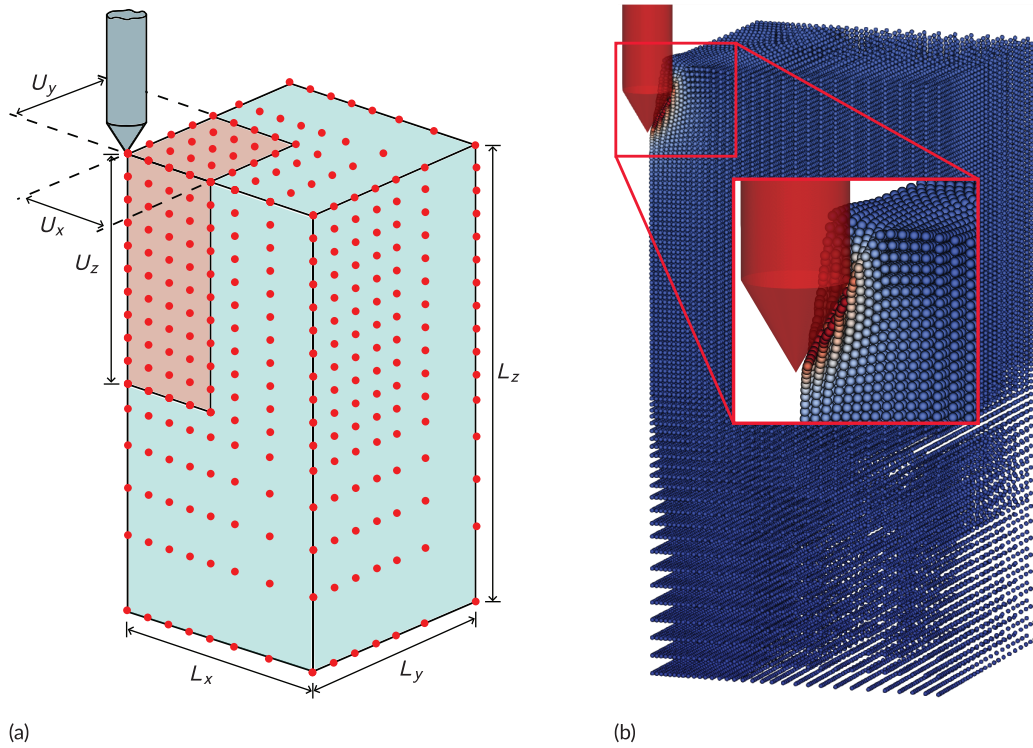


FIGURE 11 | Cone penetration test: The initial geometry and mesh setup are shown in (a), with the CPT penetration of 1.2 m shown in (b). The displacement magnitude is shown in (b), blue is 0 m and red is 0.5 m.

TABLE 3 | Cone penetration test: Deformable domain lengths.

Dimension	L_x	L_y	L_z	U_x	U_y	U_z
Length (m)	5	5	10	2.5	2.5	5

the distances between nodes are scaled with a power law from the boundary of the red region to the end of the domain,

$$dx_{i+1} = (dx_i)^{1.3} \quad (26)$$

where dx_i is the distance between the node i and node $i - 1$ in a particular direction. An indication of this nodal distribution is outlined in Figure 11a with the red dots.

The material used in the real experiment was dry silica sand obtained from Congleton in the UK [35]. There are many sophisticated models for modeling sand; however, from the justifications and results observed in Bird et al. [1] for modeling CPTs, a linear-elastic, perfectly-plastic material with a Drucker-Prager yield surface is sufficient. All the properties for the Drucker-Prager yield surface can be determined using the equations provided by Brinkgreve et al. [36], and for an overview of the use of the equations see Bird et al. [1]. However, the initial state of the material due to gravity also has to be considered, and hence, the Young's modulus will vary with depth. If a negligible cohesion is assumed (here we use $c = 300$ Pa), the variation of the Young's modulus can be determined using the formula provided by Schanz et al. [37].

$$E_{50} = E_{50}^{\text{ref}} \left(\frac{\sigma_v K_0}{p^{\text{ref}}} \right)^{m_E} \quad \text{with} \quad \sigma_v = d_p \rho \quad (27)$$

TABLE 4 | Cone penetration test: Material properties.

Property	38%	44%	82%
Reference Young's modulus, E_{50}^{ref} (kPa)	22 800	26 400	49 200
Density, ρ (kN/m ³)	16.5	16.7	18.2
Poisson's ratio	0.3	0.3	0.3
Friction angle (°)	32.8	33.5	38.3
Dilation angle (°)	2.8	3.5	8.3
Apparent cohesion (kPa)	0.3	0.3	0.3
Coefficient of earth pressure at rest, K_0	0.45	0.44	0.38
Stiffness exponent, m_E	0.58	0.57	0.44

where $K_0 = 1 - \sin(\phi)$ is the coefficient of earth pressure at rest [38], σ_v is the vertical stress and d_p is the distance of the MP from the surface of the sample (i.e., the depth), m_E is an exponent controlling the variation of stiffness [36]. Here, two relative densities are considered, 38% and 82%, with the values of their material properties provided in Table 4, alongside 44%, which is used in Section 6.4.

The normal and tangential contact penalties are respectively $50E_p$ and $25E_p$, where p is the GIMP that is contact with the material point. This variation in the penalties is required since the material has an inhomogeneous Young's modulus, and the variation enables a more accurate representation of the conduct boundary conditions without making the non-linear solver unstable through an excessively high penalty.

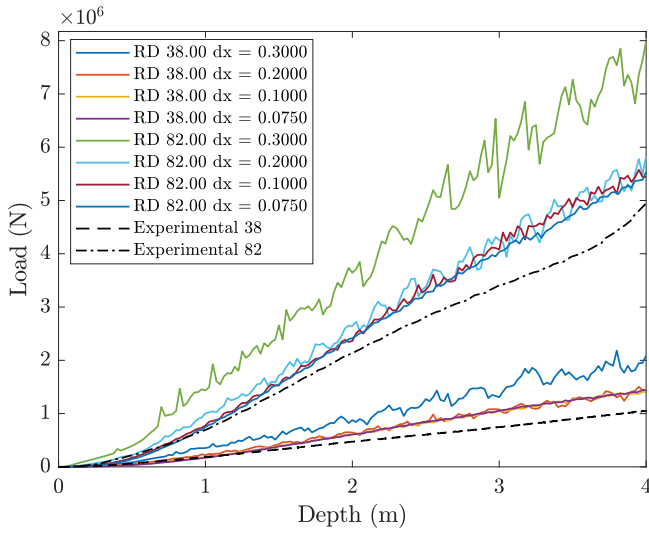


FIGURE 12 | Cone penetration test: Results for CPT tip load with depth.

6.3.3 | Results Discussion

The results for the CPT tip load with depth are shown in Figure 12 for a range of refinements, $dx = \{0.075, 0.1, 0.2, 0.3\}$ m.

Figure 12 shows that for the most refined mesh, $dx = 0.075$ m, good agreement is obtained for both relative densities. It is important to note that these results are pure predictions, and there is no tuning of the parameters for the material model or numerical parameters performed to obtain a better agreement. It is also observed that with refinement, the solutions converge in the same direction towards the experimental result, and in addition, the magnitude of the oscillations also decreases. The most likely cause for the oscillations is material points coming in and out of contact with the cone. With refinement each GIMP in contact carries a smaller portion of the load and therefore has a smaller effect on the global response.

6.4 | Plough

6.4.1 | Example Scope

The final problem considered is the modeling of a seabed cable plough, with the geometry shown in Figure 13. The plough is pulled through dry sand at a constant speed and depth. The required horizontal pull (or tow) force predicted by the numerical model is compared to the steady state experimental data obtained by Robinson et al. [39] in a 50g geotechnical centrifuge. To simplify the numerical analysis, the numerical model considers the full-scale problem at 1g, which the centrifuge represents. Following the scaling analysis for dry sand by Robinson et al. [40], this means that both length and time are scaled equally, hence the plough is pulled the full scale length but at the model speed. The experiment in [39] reaches an equilibrium in both plough depth and pull force. Here, the plough will be fixed at the recorded plough depth, and the pull force will be compared to the experimental steady state force.

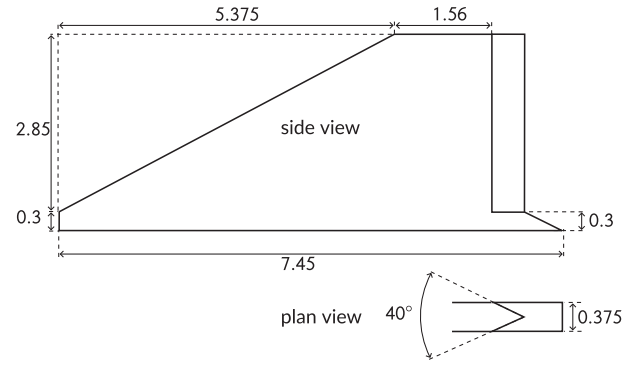


FIGURE 13 | Plough: Dimensioned drawing of the plough, metres.

6.4.2 | Setup

The numerical setup for modeling the full plough is shown in Figure 14 with the geometry of the plough provided in Figure 13 and corresponding dimension values in Table 5.

The distribution of the initial Cartesian mesh is outlined in Figure 14, where the red dots show the initial distribution of the element nodes on the boundary of the mesh. To reduce the computational cost, only half the problem is modeled, achieved using symmetric boundary conditions in x . The purpose of the initial mesh is primarily to set up the initial material point distribution. As the plough travels through the domain, the mesh, but not the material points, is adaptively refined and recovered to reduce the cost associated with the linear solve. In the red regions, the nodes are uniformly distributed with a spacing of dx m. In the blue region, the node spacing is not uniform and is subject to the power law

$$dx_{x+1} = (dx_i)^{1.3} \quad (28)$$

where dx_i is the distance between node i and $i - 1$ and $dx_1 = dx$. If a node does land exactly on the boundary of the domain, then the nearest node created by the power law series is snapped to the domain boundary. The node distribution is such that the highest density of nodes and material points is around the nose of the plough, marked A, where the most complicated 3D displacements occur. Elsewhere, where the displacement field is more 2D, such as at the main wedge of the plough, there is a greater refinement in the x and y directions compared to the z direction. This is obtained through the refined region marked B in Figure 14. The material that is not in contact with the plough has only a coarse refinement. Lastly, the sizes of the refined region sizes will depend slightly on the values of dx so that all elements in this region are equally sized. This can be expressed by the following equation

$$\bar{U} = \left[\frac{U}{dx} \right] dx \quad (29)$$

where U is the desired size of the refined region and \bar{U} is the actual size. The initial number of GIMPs per elements is 8, with a $2 \times 2 \times 2$ equally spaces configuration.

On all faces, a roller boundary condition is applied, except on the top face where a homogeneous Neumann boundary exists, and on the face marked C, see Figure 14. On the face C, a Signorini boundary condition exists so that material can move away

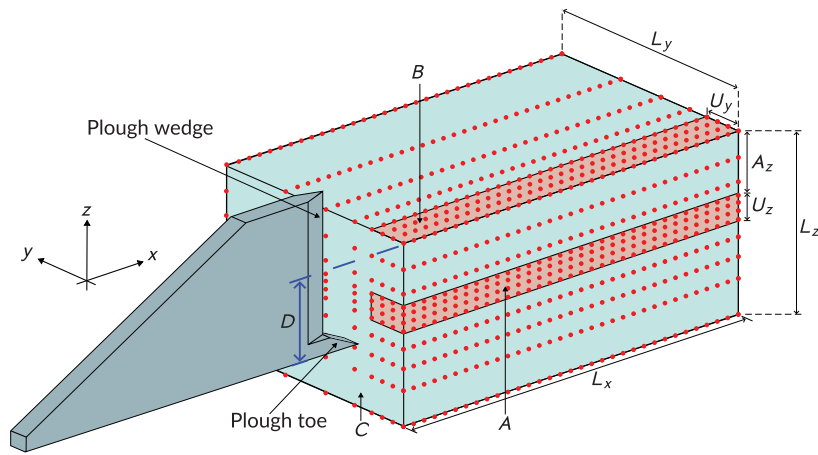


FIGURE 14 | Plough: Initial numerical setup of a plough being pulled through dry sand.

TABLE 5 | Plough: Deformable domain length.

Dimension	L_x	L_y	L_z	U_y	A_z	U_z	D
Length (m)	20	10	7.5	1.875	1.725	0.25	1.85

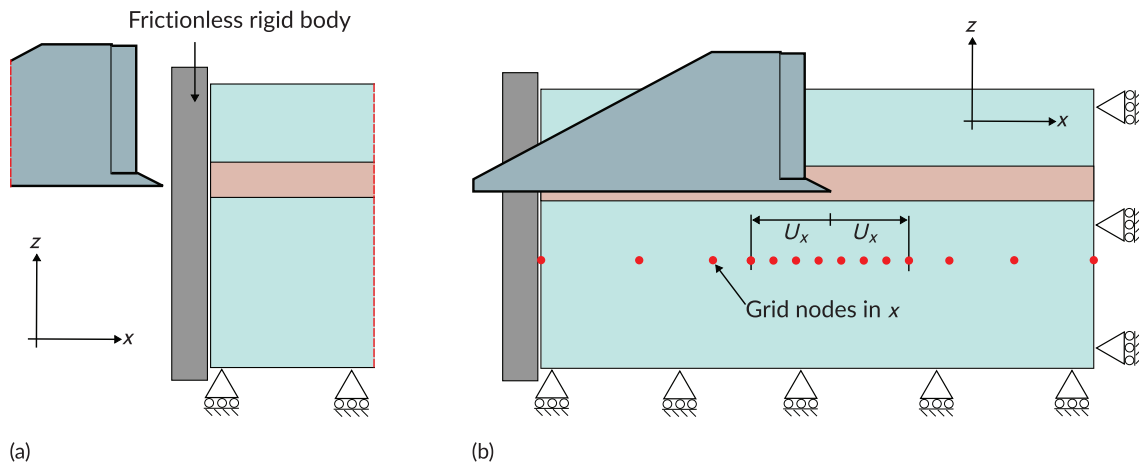


FIGURE 15 | Plough: (a) Side view of Signorini boundary conditions with adaptive refinement in x shown in (b).

from the domain boundary but cannot move across it. Pragmatically, this is enforced with a second rigid body with no friction as shown in Figure 15a. The plough was incremented at a step size of 0.025 m, and there was no interaction between the plough and the secondary rigid body.

In initial testing, it was observed that the majority of the deformation was occurring at the front of the plough, therefore, to reduce the computational cost of the simulation, mesh adaptation was developed in x as the plough moved through the domain, as shown in Figure 15b. About the tip of the plough, in both the positive and negative directions, a region with $U_x = 0.5$ m was uniformly refined. Outside this region, the power law described with Equation (28) was used. To prevent the rigid body penetrating GIMPs all edges with an angle convex edges with an angle less than 90° were filleted with a radius equal to the minimum side half length of the GIMP, there were approximately 10 segments per 90° of fillet.

6.4.3 | Results Discussion

Here, the numerical results for the plough tow force are compared to the equivalent centrifuge experiment, [40], and additionally, the performance of the numerical algorithm is discussed. In the previous sections, the geometry of the rigid bodies was relatively simple, and in addition, the point of the CPT coincided with the edge of the domain, so there was no risk of the rigid body going inside a material point. For this problem, however, the plough contains many surfaces which are connected via rounded concave and convex edges.

Three mesh sizes were considered, $dx = \{0.075, 0.15, 0.2\}$ m, and the results of the plough tow force with plough positions are shown in Figure 16 alongside the experimental data. The primary observation from the numerical results is that with increasing refinement, the tow force gets closer to the experiment, with generally good agreement obtained between mesh sizes

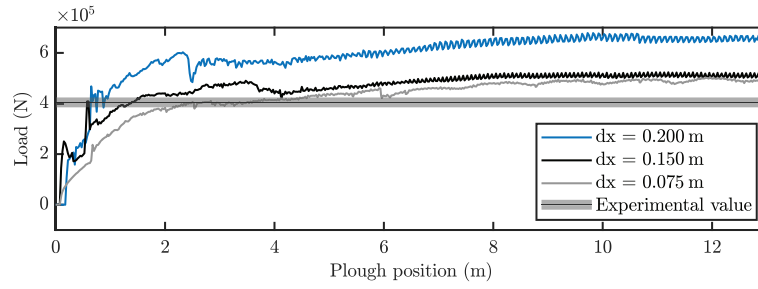


FIGURE 16 | Plough: Comparison of numerical results for pull load with plough position against experimental data for three mesh refinements.

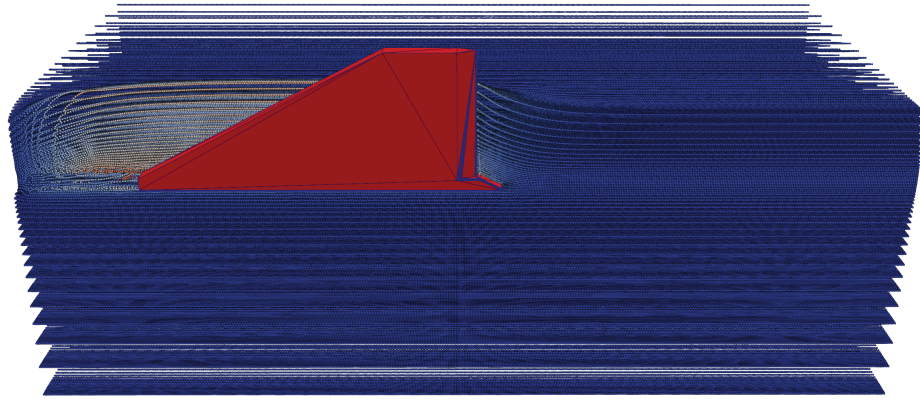


FIGURE 17 | Plough: Deformed GIMP positions colored according to the x displacement (red is 3 m, blue is 0 m) for a plough embedded 10 m into the material for the refinement $dx = 0.075$ m.

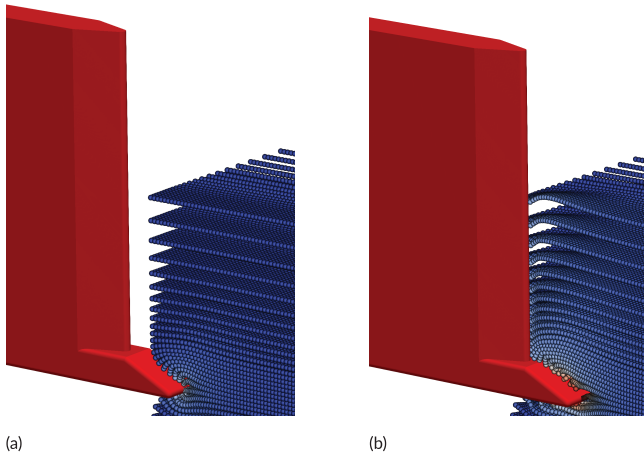


FIGURE 18 | Plough: Deformed GIMP positions colored according to the x displacement (red is 1 m, blue is 0 m) for a plough just before (a) and just after, (b) the front wedge is embedded. (a) Just before, (b) Just after.

$dx \in \{0.075, 0.15\}$ m and the experimental results (Figure 17). The trend of the numerical results being consistently slightly higher than those observed experimentally is consistent with the CPT problem results, and again, the simulation is purely predictive, and no adjustments to the material or numerical parameters were performed. It is also likely that reducing relative density could close the distance between the results. Before 7.45 m, the plough is embedding itself into the domain from the side. In this

initial region, $0 \rightarrow 7.45$ m, the results are the most chaotic with sudden changes in the force caused by the buildup of material in front of the plough from the initial embedment. Additionally, there are sharp peaks in the load caused by the different parts of the plough coming into contact with the domain. For example, the greyed region in Figure 16 is the plough wedge first coming into contact, going from Figure 18a,b.

The plough is the most complex geometry considered in this paper, and it is therefore appropriate to comment on the stability of this problem. For all meshes, the plough was incremented by 0.025 m each time step. If the time step failed to converge, the step size was reduced by a factor of 2 and restarted. The displacement increment sizes were recorded for each mesh size and are plotted in Figure 19. The figure shows that for all meshes the algorithm remained stable for all mesh sizes, with only $dx = 0.075$ m requiring a reduction in the displacement step size. This shows that not only was good agreement with experimental data achieved, but the algorithms presented here are robust and reliable.

7 | Conclusion

This paper provides a new 3D large deformation contact formulation for modeling the interaction between deformable and rigid bodies. The method uses the definition of the GIMP domain to impose point-to-surface contact between the vertices of the

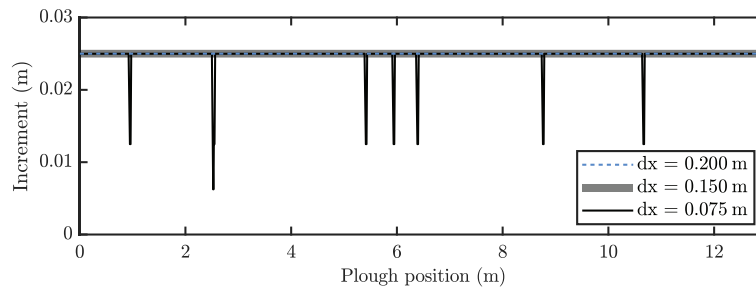


FIGURE 19 | Plough: Comparison of successful load increment sizes for the three mesh sizes.

GIMP domains and the surface of the rigid body. Importantly, no additional boundary reconstruction is necessary, and the contact constraints are applied consistently with the numerical representation of the extent of the physical material. This is important—it has been demonstrated that the correct stress field at the contact boundary is recovered only when the contact conditions are applied consistently (confirming the 2D result of Bird et al. [1]). As each of the vertices of the GIMP domain can individually be in contact with the rigid body, the possibility of a material point being undetected when interacting with a locally concave rigid body is significantly reduced. This paper has also introduced a new energy minimization domain updating approach at the converged state at the end of each time step. The approach maintains that the final extent of the physical material represented by each material point domain is consistent with the energy in the contact penalty spring at the converged state. If the material point domains were updated without this consideration, large spurious material point domain-rigid body overlaps and therefore contact penalty spring forces (and additional energy) could be generated, leading to physically questionable and numerically unstable simulations. The frictional interaction between the deformable and rigid bodies was validated using the analytical solution of a sphere rolling down a slope. This validated both the normal and the frictional contact, modeled using Coulomb friction, for a rigid body that was free to move. To validate the formulation for example practical problems, two in the area of soil-structure interaction were chosen, with comparisons made against experimental results obtained from a geotechnical centrifuge, there being no analytical solutions. This included the load on the end of the cone for a CPT and the tow force required to pull a plough at a fixed depth through sand. Both agreed well with experimental data, and both saw convergence towards the experimental result with refinement. The numerical results were based on a purely predictive methodology, i.e., the material constitutive parameters were not tuned to match the experimental results, implying that the method can be reliably used to interpolate within and extrapolate beyond the physical dataset. Additionally, it was demonstrated for the plough that the solution methodology was stable for difficult contact problems with concave geometries.

Acknowledgments

This work was supported by the Engineering and Physical Sciences Research Council [Grant Nos. EP/W000970/1, EP/W000997/1, and EP/W000954/1]. The second author was supported by funding from the Faculty of Science, Durham University. All data created during this research are openly available at <https://doi.org/10.15128/r27d278t149>.

Data Availability Statement

All data created during this research are openly available at <https://doi.org/10.15128/r27d278t149>.

Endnotes

¹ This typically presents itself as a bouncing situation, where a contact point moves either in-and-out of the rigid body or between the red and green region.

References

1. R. E. Bird, G. Pretti, W. M. Coombs, et al., “An Implicit Material Point-To-Rigid Body Contact Approach for Large Deformation Soil–Structure Interaction,” *Computers and Geotechnics* 174 (2024): 106646.
2. D. Sulsky, Z. Chen, and H. L. Schreyer, “A Particle Method for History-Dependent Materials,” *Computer Methods in Applied Mechanics and Engineering* 118, no. 1–2 (1994): 179–196.
3. W. T. Solowski, M. Berzins, W. M. Coombs, et al., “Material Point Method: Overview and Challenges Ahead,” in *Advances in Applied Mechanics*, vol. 54 (Elsevier, 2021), 113–204.
4. A. de Vaucorbeil, V. P. Nguyen, S. Sinaie, and J. Y. Wu, “Material Point Method After 25 Years: Theory, Implementation, and Applications,” in *Advances in Applied Mechanics*, vol. 53 (Elsevier, 2020), 185–398.
5. J. L. Gonzalez Acosta, P. J. Vardon, and M. A. Hicks, “Development of an Implicit Contact Technique for the Material Point Method,” *Computers and Geotechnics* 130 (2021): 103859.
6. G. Pretti, “Continuum Mechanics and Implicit Material Point Method to Underpin the Modelling of Drag Anchors for Cable Risk Assessment. PhD Thesis, Durham University,” 2024.
7. K. Nakamura, S. Matsumura, and T. Mizutani, “Particle-To-Surface Frictional Contact Algorithm for Material Point Method Using Weighted Least Squares,” *Computers and Geotechnics* 134 (2021): 104069.
8. Z. Lei, B. Wu, S. Wu, Y. Nie, S. Cheng, and C. Zhang, “A Material Point-Finite Element (MPM-FEM) Model for Simulating Three-Dimensional Soil-Structure Interactions With the Hybrid Contact Method,” *Computers and Geotechnics* 152 (2022): 105009.
9. M. Martinelli and G. Vahid, “Investigation of the Material Point Method in the Simulation of Cone Penetration Tests in Dry Sand,” *Computers and Geotechnics* 130 (2021): 103923.
10. S. G. Bardenhagen and E. M. Kober, “The Generalized Interpolation Material Point Method,” *Computer Modeling in Engineering and Sciences* 5, no. 6 (2004): 477–496.
11. R. Tielen, E. Wobbes, M. Möller, and L. Beuth, “A High Order Material Point Method,” *Procedia Engineering* 175 (2017): 265–272. Proceedings of the 1st International Conference on the Material Point Method (MPM 2017).
12. P. Wriggers, *Computational Contact Mechanics* (Springer, 2006).

13. W. M. Coombs and C. E. Augarde, "AMPLE: A Material Point Learning Environment," *Advances in Engineering Software* 139 (2020): 102748.
14. T. J. Charlton, W. M. Coombs, and C. E. Augarde, "iGIMP: An Implicit Generalised Interpolation Material Point Method for Large Deformations," *Computers & Structures* 190 (2017): 108–125.
15. J. Simo, "Algorithms for Static and Dynamic Multiplicative Plasticity That Preserve the Classical Return Mapping Schemes of the Infinitesimal Theory," *Computer Methods in Applied Mechanics and Engineering* 99, no. 1 (1992): 61–112.
16. E. A. de Souza Neto, D. Peric, and D. R. J. Owen, *Computational Methods for Plasticity: Theory and Applications* (John Wiley & Sons, Ltd, 2008).
17. W. M. Coombs, C. E. Augarde, A. J. Brennan, et al., "On Lagrangian Mechanics and the Implicit Material Point Method for Large Deformation Elasto-Plasticity," *Computer Methods in Applied Mechanics and Engineering* 358 (2020): 112622.
18. M. Cortis, W. M. Coombs, C. E. Augarde, M. Brown, A. Brennan, and S. Robinson, "Imposition of Essential Boundary Conditions in the Material Point Method," *International Journal for Numerical Methods in Engineering* 113, no. 1 (2018): 130–152.
19. L. Wang, W. M. Coombs, C. E. Augarde, et al., "An Efficient and Locking-Free Material Point Method for Three-Dimensional Analysis With Simplex Elements," *International Journal for Numerical Methods in Engineering* 122, no. 15 (2021): 3876–3899.
20. L. Wang, W. M. Coombs, C. E. Augarde, et al., "On the Use of Domain-Based Material Point Methods for Problems Involving Large Distortion," *Computer Methods in Applied Mechanics and Engineering* 355 (2019): 1003–1025.
21. B. Chandra, V. Singer, T. Teschemacher, R. Wüchker, and A. Larese, "Nonconforming Dirichlet Boundary Conditions in Implicit Material Point Method by Means of Penalty Augmentation," *Acta Geotechnica* 16 (2021): 2315–2335.
22. Y. Bing, M. Cortis, T. J. Charlton, W. M. Coombs, and C. E. Augarde, "B-Spline Based Boundary Conditions in the Material Point Method," *Computers & Structures* 212 (2019): 257–274.
23. V. Singer, T. Teschemacher, A. Larese, R. Wüchker, and K. U. Bletzinger, "Lagrange Multiplier Imposition of Non-Conforming Essential Boundary Conditions in Implicit Material Point Method," *Computational Mechanics* 73 (2024): 1311–1333.
24. M. A. Crisfield, "Non-Linear Finite Element Analysis of Solids and Structures," in *Advanced Topics*, vol. 2 (Wiley, 1997).
25. J. U. Brackbill and H. M. Ruppel, "FLIP: A Method for Adaptively Zoned, Particle-In-Cell Calculations of Fluid Flows in Two Dimensions," *Journal of Computational Physics* 65, no. 2 (1986): 314–343.
26. E. Burman, "Ghost Penalty," *Comptes Rendus Mathématique* 348, no. 21 (2010): 1217–1220.
27. W. M. Coombs, "Ghost Stabilisation of the Material Point Method for Stable Quasi-Static and Dynamic Analysis of Large Deformation Problems," *International Journal for Numerical Methods in Engineering* 124, no. 21 (2023): 4841–4875.
28. E. N. Dvorkin and M. B. Goldschmit, *Nonlinear Continua* (Springer Science & Business Media, 2006).
29. G. Pietrzak and A. Curnier, "Large Deformation Frictional Contact Mechanics: Continuum Formulation and Augmented Lagrangian Treatment," *Computer Methods in Applied Mechanics and Engineering* 177, no. 3–4 (1999): 351–381.
30. N. Ottosen and H. Petersson, *Introduction to the Finite Element Method* (Prentice-Hall, 1992).
31. A. Curnier, Q. He, and A. Klarbring, "Continuum Mechanics Modelling of Large Deformation Contact With Friction," in *Contact Mechanics* (Springer, 1995), 145–158.
32. K. Poullos and Y. Renard, "An Unconstrained Integral Approximation of Large Sliding Frictional Contact Between Deformable Solids," *Computers & Structures* 153 (2015): 75–90.
33. A. Popp, M. W. Gee, and W. A. Wall, "A Finite Deformation Mortar Contact Formulation Using a Primal–Dual Active Set Strategy," *International Journal for Numerical Methods in Engineering* 79, no. 11 (2009): 1354–1391.
34. R. Bird, W. M. Coombs, C. Augarde, et al., "Cone Penetration Tests (CPTs) in Layered Soils: A Material Point Approach," in *Proceedings of the 10th European Conference on Numerical Methods in Geotechnical Engineering (NUMGE 2023)* (International Society for Soil Mechanics and Geotechnical Engineering, 2023), 145–158.
35. C. Davidson, M. Brown, B. Cerfontaine, et al., "Physical Modelling to Demonstrate the Feasibility of Screw Piles for Offshore Jacket Supported Wind Energy Structures," *Géotechnique* 72, no. 2 (2022): 108–126.
36. R. B. J. Brinkgreve, E. Engin, and H. K. Engin, "Validation of Empirical Formulas to Derive Model Parameters for Sands," *Numerical Methods in Geotechnical Engineering* 137 (2010): 142.
37. T. Schanz, P. A. Vermeer, and P. G. Bonnier, "The Hardening Soil Model: Formulation and Verification," in *Beyond 2000 in Computational Geotechnics* (Routledge, 2019), 281–296.
38. J. Jaky, "The Coefficient of Earth Pressure at Rest," *Journal of the Society of Hungarian Architects and Engineers* 78, no. 22 (1944): 5335–5357.
39. S. Robinson, M. J. Brown, H. Matsui, et al., "A Cone Penetration Test (CPT) Approach to Cable Plough Performance Prediction Based Upon Centrifuge Model Testing," *Canadian Geotechnical Journal* 58, no. 10 (2021): 1466–1477.
40. S. Robinson, M. J. Brown, H. Matsui, et al., "Centrifuge Testing to Verify Scaling of Offshore Pipeline Ploughs," *International Journal of Physical Modelling in Geotechnics* 19, no. 6 (2019): 305–317.

Appendix A

Rigid Body First and Second Variations

This appendix provides the first and second variations of a point on a triangle surface, \mathbf{x}' . The definition from Equation (10) is repeated here, with a slight abuse of the sum notation,

$$\mathbf{x}' = N(\xi)\mathbf{G}(\theta) = (\mathbf{A}\mathbf{R} + \mathbf{B}\mathbf{I}) \cdot \mathbf{t}_{RB} + \mathbf{x}_M \quad (\text{A1})$$

Its first variation is

$$\delta\mathbf{x}' = \frac{\partial N(\xi)}{\partial \xi^\alpha} \delta \xi^\alpha \mathbf{G}(\theta) + N(\xi) \frac{\partial \mathbf{G}(\theta)}{\partial \theta} \cdot \delta\theta \quad (\text{A2})$$

and second variation

$$\begin{aligned} \Delta\delta\mathbf{x}' = & \underbrace{\frac{\partial N(\xi)}{\partial \xi^\alpha} \Delta\delta \xi^\alpha \mathbf{G}(\theta)}_{:= \mathbf{t}_a \Delta\delta \xi^\alpha} + \underbrace{\frac{\partial N(\xi)}{\partial \xi^\alpha} \delta \xi^\alpha \frac{\partial \mathbf{G}(\theta)}{\partial \theta} \cdot \Delta\theta}_{:= \left(\frac{\partial(\Delta\mathbf{x}')}{\partial \xi^\beta} \right) \delta \xi^\alpha} \\ & + \underbrace{\frac{\partial N(\xi)}{\partial \xi^\alpha} \Delta \xi^\alpha \frac{\partial \mathbf{G}(\theta)}{\partial \theta} \cdot \delta\theta}_{:= \left(\frac{\partial(\delta\mathbf{x}')}{\partial \xi^\beta} \right) \Delta \xi^\alpha} + \underbrace{N(\xi) \Delta\theta \cdot \frac{\partial^2 \mathbf{G}(\theta)}{\partial \theta^2} \cdot \delta\theta}_{:= \delta\theta \left(\frac{\partial^2 \mathbf{x}'}{\partial \theta^2} \right) \cdot \Delta\theta} \quad (\text{A3}) \end{aligned}$$

which requires the following definitions,

$$\frac{\partial(\delta\mathbf{x}')}{\partial \xi^\beta} = \delta \left(\frac{\partial \mathbf{x}'}{\partial \xi^\beta} \right) \quad \text{and} \quad \frac{\partial(\Delta\mathbf{x}')}{\partial \xi^\beta} = \Delta \left(\frac{\partial \mathbf{x}'}{\partial \xi^\beta} \right) \quad (\text{A4})$$

and

$$\Delta \left(\frac{\partial(\delta\mathbf{x}')}{\partial \xi^\beta} \right) = \frac{\partial N(\xi)}{\partial \xi^\beta} \Delta\theta \cdot \frac{\partial^2 \mathbf{G}(\theta)}{\partial \theta^2} \cdot \delta\theta \quad (\text{A5})$$

Additionally, Equations (A2) and (A3) are dependent on the first and second variations of $\mathbf{G}(\theta)$, respectively given as

$$\frac{\partial \mathbf{G}_n(\theta)}{\partial \theta} \cdot \delta \theta = (\mathbf{A}_n \mathbf{R} + \mathbf{B}_n \mathbf{I}) \cdot \delta \mathbf{t}_{RB} + \delta \mathbf{x}_M \quad (\text{A6})$$

and

$$\Delta \theta \cdot \frac{\partial^2 \mathbf{G}_n(\theta)}{\partial \theta^2} \cdot \delta \theta = (\mathbf{A}_n \mathbf{R} + \mathbf{B}_n \mathbf{I}) \cdot \Delta \delta \mathbf{t}_{RB} \quad (\text{A7})$$

Furthermore the first and second variation of \mathbf{t}_{RB} are also required, respectively,

$$\delta \mathbf{t}_{RB} = \left(\frac{\mathbf{I} - \mathbf{t}_{RB} \otimes \mathbf{t}_{RB}}{\|\mathbf{v}\|} \right) \cdot \frac{\partial \mathbf{v}}{\partial t} \delta t = \left(\frac{\mathbf{I} - \mathbf{t}_{RB} \otimes \mathbf{t}_{RB}}{\|\mathbf{v}\|} \right) \cdot \delta \mathbf{v} \quad (\text{A8})$$

where $\mathbf{v} = \mathbf{x}_D - \mathbf{x}_M$

and

$$\begin{aligned} \Delta \delta \mathbf{t}_{RB} &= \Delta \left[\left(\frac{\mathbf{I} - \mathbf{t}_{RB} \otimes \mathbf{t}_{RB}}{\|\mathbf{v}\|} \right) \cdot \delta \mathbf{v} \right] \\ &= \Delta \left(\frac{1}{\|\mathbf{v}\|} \right) (\mathbf{I} - \mathbf{t}_{RB} \otimes \mathbf{t}_{RB}) \cdot \delta \mathbf{v} \\ &\quad + \left(\frac{1}{\|\mathbf{v}\|} \right) (\mathbf{I} - \Delta \mathbf{t}_{RB} \otimes \mathbf{t}_{RB}) \cdot \delta \mathbf{v} \\ &\quad + \left(\frac{1}{\|\mathbf{v}\|} \right) (\mathbf{I} - \mathbf{t}_{RB} \otimes \Delta \mathbf{t}_{RB}) \cdot \delta \mathbf{v} \end{aligned} \quad (\text{A9})$$

where

$$\Delta \left(\frac{1}{\|\mathbf{v}\|} \right) = \frac{-\mathbf{v}}{\|\mathbf{v}\|^3} \cdot \Delta \mathbf{v} \quad \text{and} \quad \Delta \mathbf{t}_{RB} = \left(\frac{\mathbf{I} - \mathbf{t}_{RB} \otimes \mathbf{t}_{RB}}{\|\mathbf{v}\|} \right) \cdot \Delta \mathbf{v}$$

Appendix B

Contact First and Second Variations

To complete the description of the normal and the tangential contact, it is necessary to have their linearizations, which are required for the implicit solve.

Variation of Normal Contact Residual

The residual for the normal contact, from Equation (17), repeated here for readability, is

$$\delta U_N = \int_{\psi_i(I) \cap \delta(\mathbf{x}')} (\delta g_N \epsilon_N g_N) \, d\mathbf{x} \quad (\text{B1})$$

where $\mathbf{p}_N = \epsilon_N \mathbf{n} g_N$ from Equation (18). Linearizing (B1) gives the gradient of the residual, necessary for the Newton-Raphson scheme,

$$\Delta \delta U_N = \int_{\psi_i(I) \cap \delta(\mathbf{x}')} (\Delta(\delta g_N) \epsilon_N g_N + \delta g_N \Delta(\epsilon_N g_N)) \, d\mathbf{x} \quad (\text{B2})$$

where δg_N , $\Delta(\delta g_N)$ and $\Delta(\epsilon_N g_N)$ are defined below. Following closely the work of Pietrzak and Curnier [29], and Wriggers [12], the forms of the first and second variations of the gap functions can be provided. The gap function, (14), is restated here for convenience

$$g_N = [\mathbf{x}(\tau) - \mathbf{x}'(\xi(\tau)^\alpha, \tau)] \cdot \mathbf{n} \quad (\text{B3})$$

where \mathbf{x} is the point, the vertex of the GIMP domain, in contact with the rigid body surface at time τ , where $\xi^\alpha(\tau)$, $\alpha \in \{1, 2\}$, is a function describing the local position of the CPP projection onto the surface that is used to describe the global contact position \mathbf{x}' . The first variation of the gap function is

$$\delta g_N = [\delta \mathbf{x} - \delta \mathbf{x}'] \cdot \mathbf{n} \quad (\text{B4})$$

where δ denotes the first variation. The second variation of the normal gap g_N is

$$\begin{aligned} \Delta \delta g_N &= -\mathbf{n} \cdot \left(\frac{\partial(\delta \mathbf{x}')}{\partial \xi^\alpha} \Delta \xi^\alpha + \frac{\partial(\Delta \mathbf{x}')}{\partial \xi^\alpha} \delta \xi^\alpha + \delta \theta \cdot \left(\frac{\partial^2 \mathbf{x}'}{\partial \theta^2} \right) \cdot \Delta \theta \right) \\ &\quad + g_N \mathbf{n} \cdot \left(\frac{\partial(\delta \mathbf{x}')}{\partial \xi^\alpha} \right) A^{\alpha\beta} \left(\frac{\partial(\Delta \mathbf{x}')}{\partial \xi^\beta} \right) \cdot \mathbf{n} \end{aligned} \quad (\text{B5})$$

where ξ^α is the local coordinate on a triangular element of the rigid body, with its first variations $\delta \xi$ or $\Delta \xi$, and

$$[A^{\alpha\beta}]^{-1} = [A_{\alpha\beta}] = \mathbf{t}_\alpha \cdot \mathbf{t}_\beta$$

is the inverse of the first fundamental form matrix.

Variation of the Tangential Contact Residual

The tangent residual, Equation (17), is

$$\delta U_T = \int_{\psi_i(I) \cap \delta(\mathbf{x}')} (\delta \xi^\alpha \mathbf{t}_\alpha \cdot \mathbf{p}_T) \, d\mathbf{x} \quad (\text{B6})$$

where \mathbf{p}_T is the tangential pressure that acts to resist sliding motion contact. Similarly to the normal contact, linearizing (B6) gives

$$\Delta \delta U_T = \int_{\psi_i(I) \cap \delta(\mathbf{x}')} (\Delta(\delta \xi^\alpha) \mathbf{t}_\alpha \cdot \mathbf{p}_T + \delta \xi^\alpha \Delta(\mathbf{t}_\alpha \cdot \mathbf{p}_T)) \, d\mathbf{x} \quad (\text{B7})$$

where $\Delta(\delta \xi^\alpha)$ and $\Delta(\mathbf{t}_\alpha \cdot \mathbf{p}_T)$ are defined below. The local coordinate $\xi^\alpha(\tau)$ is a function of the CPP; its first and second variations are therefore not trivial. The first variation is

$$\delta \xi^\alpha = A^{\alpha\beta} \left[(\delta \mathbf{x} - \delta \mathbf{x}') \cdot \mathbf{t}_\beta + g_N \mathbf{n} \cdot \frac{\partial(\delta \mathbf{x}')}{\partial \xi^\beta} \right] \quad (\text{B8})$$

and the corresponding second variation is

$$\begin{aligned} \Delta \delta \xi^\alpha &= A^{\alpha\beta} \left[-\mathbf{t} \cdot \left(\delta \xi^\sigma \frac{\partial(\Delta \mathbf{x}')}{\partial \xi^\sigma} + \Delta \xi^\gamma \frac{\partial(\delta \mathbf{x}')}{\partial \xi^\gamma} + \delta \theta \left(\frac{\partial^2 \mathbf{x}'}{\partial \theta^2} \right) \Delta \theta \right) \right. \\ &\quad - \delta \xi^\gamma \mathbf{t}_\gamma \left(\frac{\partial(\Delta \mathbf{x}')}{\partial \xi^\beta} \right) - \Delta \xi^\gamma \mathbf{t}_\gamma \left(\frac{\partial(\delta \mathbf{x}')}{\partial \xi^\beta} \right) \\ &\quad + (\delta \mathbf{x} - \delta \mathbf{x}') \frac{\partial(\Delta \mathbf{x}')}{\partial \xi^\beta} + (\Delta \mathbf{x} - \Delta \mathbf{x}') \frac{\partial(\delta \mathbf{x}')}{\partial \xi^\beta} \\ &\quad \left. + g_N \mathbf{n} \cdot \Delta \left(\frac{\partial(\delta \mathbf{x}')}{\partial \xi^\beta} \right) \right] \end{aligned} \quad (\text{B9})$$

Stick and Slip

The first variation of the frictional force in the tangential direction, $\mathbf{t}_\alpha \cdot \mathbf{p}_T$, is required in Equation (B7). The variation of \mathbf{p}_T is a function of the discretization of the movement of a point over the surface, the friction law, and the friction state (slip or stick). Therefore, first, the total tangential movement over the discrete time step $m+1$ is defined as

$$\begin{aligned} \dot{\mathbf{g}}_T \Delta t &\approx \mathbf{g}_{T,m+1} - \mathbf{g}_{T,m}^m \\ &= \mathbf{t}_{\alpha,m+1} \Delta \xi^\alpha = \mathbf{t}_{\alpha,m+1} (\xi_{m+1}^\alpha - \xi_m^\alpha) \\ &= \Delta \mathbf{g}_T \end{aligned} \quad (\text{B10})$$

Next, the elastic trial stick state can be defined as

$$\mathbf{p}_{\text{tr}} = \epsilon_T (\mathbf{g}_{T,m+1} - \mathbf{g}_{\text{slip},m}) = \mathbf{p}_{T,m} + \epsilon_T \Delta \mathbf{g}_T \quad (\text{B11})$$

where $(\mathbf{g}_{T,m+1} - \mathbf{g}_{\text{slip},m})$ is the trial stick movement that has occurred, $\mathbf{p}_{T,m}$ is the previously converged tangential friction vector. The right-hand side of Equation (B11) is possible as μ in Equation (21) is constant [1, 12]. With these definitions, the trial stick state is used with yield surface (21)

to determine if the contact is in a stick or slip state, and subsequently, the frictional force can be calculated using

$$\mathbf{p}_T = \begin{cases} \mathbf{p}_{tr} & \text{if } \|\mathbf{p}_{tr}\| \leq \mu|\mathbf{p}_N|, \text{ stick} \\ \mu|\mathbf{p}_N|(\mathbf{p}_{tr}/\|\mathbf{p}_{tr}\|) & \text{if } \|\mathbf{p}_{tr}\| > \mu|\mathbf{p}_N|, \text{ slip} \end{cases} \quad (\text{B12})$$

With the above definitions the variation of $\mathbf{t}_\alpha \cdot \mathbf{p}_T$ can be defined. Starting generally, the first variation is

$$\Delta(\mathbf{t}_\alpha \cdot \mathbf{p}_T) = [(\Delta\mathbf{t}_\alpha) \cdot \mathbf{p}_T] + [\mathbf{t}_\alpha \cdot (\Delta\mathbf{p}_T)] \quad (\text{B13})$$

The $\Delta\mathbf{t}_\alpha$ term is simply,

$$\Delta\mathbf{t}_\alpha = \frac{\partial(\Delta\mathbf{x}')}{\partial\xi^\alpha} \quad (\text{B14})$$

noting that δ and Δ are equivalent operators. The second term of (B13) requires the variation $\Delta\mathbf{p}_T$, which is either acting in stick or slip, defined in Equation (B12).

Stick

For the *stick* case, the frictional force takes the form

$$\mathbf{p}_T = \mathbf{p}_{T,m} + \epsilon_T \Delta\mathbf{g}_T = \mathbf{p}_{T,m} + \epsilon_T \mathbf{g}_T^\Delta$$

where $\Delta\mathbf{g}_T$, the total tangential movement over the surface during a time step, is redefined as \mathbf{g}_T^Δ to avoid conflicting notation with first and second variations. It is first convenient to define the variation in tangential movement,

$$\Delta\mathbf{g}_T^\Delta = (\Delta\mathbf{t}_{\alpha,m+1})(\xi_{m+1}^\alpha + \xi_m^\alpha) + \mathbf{t}_{\alpha,m+1}(\Delta\xi_{m+1}^\alpha) \quad (\text{B15})$$

This enables the definition of the first variation of the stick contact force,

$$\Delta\mathbf{p}_T = \epsilon_T \Delta\mathbf{g}_T^\Delta \quad (\text{B16})$$

Slip

For the *slip* case \mathbf{p}_T has the form

$$\mathbf{p}_T = \mu|\mathbf{p}_N| \left(\frac{\mathbf{p}_{tr}}{\|\mathbf{p}_{tr}\|} \right)$$

and its corresponding variation is

$$\Delta\mathbf{p}_T = \mu(\Delta|\mathbf{p}_N|) \left(\frac{\mathbf{p}_{tr}}{\|\mathbf{p}_{tr}\|} \right) + \mu|\mathbf{p}_N| \Delta \left(\frac{\mathbf{p}_{tr}}{\|\mathbf{p}_{tr}\|} \right) \quad (\text{B17})$$

where

$$\Delta|\mathbf{p}_N| = \epsilon_N \Delta|\mathbf{g}_N| = \epsilon_N \frac{\mathbf{g}_N}{\|\mathbf{g}_N\|} \Delta\mathbf{g}_N \quad (\text{B18})$$

and

$$\Delta \left(\frac{\mathbf{p}_{tr}}{\|\mathbf{p}_{tr}\|} \right) = \left(\frac{\mathbf{I} - \mathbf{s} \otimes \mathbf{s}}{\|\mathbf{p}_{tr}\|} \right) \cdot \Delta\mathbf{p}_{tr} \quad \text{where } \mathbf{s} = \mathbf{p}_{tr}/\|\mathbf{p}_{tr}\| \quad (\text{B19})$$

noting that $\mathbf{p}_{tr} = \mathbf{p}_{T,m} + \epsilon_T \mathbf{g}_T^\Delta$; it is the same as the stick form of \mathbf{p}_T and also therefore has the same form for the first variation.